Deciphering Interfacial Reactions via Optical Sensing to Tune the Interphase Chemistry for Optimized Na-Ion Electrolyte Formulation

Parth Desai, Jiaqiang Huang, Hussein Hijazi, Leiting Zhang, Sathiya Mariyappan, Jean- Marie Tarascon

HAL Id: hal-03318049
https://hal.science/hal-03318049

Submitted on 9 Aug 2021

Deciphering interfacial reactions via optical sensing to tune the interphase chemistry for optimized Na-ion electrolyte formulation

Parth Desai, Jiaqiang Huang, Hussein Hijazi, Leiting Zhang, Sathiya Mariyappan,[*] and Jean-Marie Tarascon[*]

P. D, Dr. J. H, Dr. H. H, Dr. S. M and Prof. J.-M. T

Chimie du Solide-Energie, UMR 8260, Collège de France, 75231 Paris Cedex 05, France

E-mail: sathiya.mariyappan@college-de-france.fr and jean-marie.tarascon@college-de-france.fr

P. D and Prof. J.-M. T

Sorbonne Université, 4 Place Jussieu, 75005, Paris, France

P. D, Dr. J. H, Dr. S. M and Prof. J.-M. T

Réseau sur le Stockage Electrochimique de l'Energie (RS2E), FR CNRS 3459, France

Dr. L. Z

Battery Electrodes and Cells, Electrochemistry Laboratory, Paul Scherrer Institute, Forschungsstrasse 111, 5232 Villigen-PSI, Switzerland

Keywords: Na-ion electrolytes, *operando* sensing, interphases, electrolyte additives, interfacial reactions

Abstract

Interphases, solid-electrolyte interphase (SEI) and cathode-electrolyte interphase (CEI) are the key influencers in determining battery life and performance. Especially, for technologies such as sodium ion batteries that are in development stage, it is crucial to tune the interphase chemistry without which it suffers at present from poor performance metrics for reaching real-life applications. In this study, we utilize optical sensors as a tool to follow *operando*, the thermal events of interfacial reactions and established the role of different electrolyte additives during the SEI/CEI formation. Using the acquired knowledge from sensing, together with complementary studies in Na-ion full-cells, we propose a new electrolyte formulation that showed stable cycling performance at 0-55 °C with very low self-discharge and improved safety due to mitigated

gassing during cycling. Finally, we nurture our studies by transferring the know-hows to prototype cylindrical 18650 cells. We hope such findings will accelerate the practical development of Na-ion batteries.

1. Introduction

Lithium ion batteries (LIBs), one of the most cherished electrochemical energy storage devices of today, are growing in demand as their usage spreads from electronic devices to electric vehicles as well as stationary applications[1]. However, limited lithium resources together with their uneven distribution in earth necessitate the development of additional complementary battery technologies to fulfil the need[2,3]. Sodium ion batteries (NIBs) that share similar chemistry as well as same production and engineering units with LIBs are expected to fill this gap and prototype NIBs have already been demonstrated by many start-up companies worldwide[4,5]. Still, NIBs lack an optimized electrolyte formulation to realize long cycle life, high safety and low self-discharge which are major requirements for reaching real-life applications[4,6].

Back in 20 years, a humongous amount of work has been carried out to reach today's electrolyte formulation for Li-ion batteries. Nevertheless the challenges still persist for moving to high voltage positive electrodes (eg. lithium layered oxides, high voltage spinels etc) for increasing the energy density, where the redox process happens well beyond the electrolyte stability window[7]. In fact, Li-ion batteries are gifted with solid electrolyte interphase (SEI) that forms by the reduction of electrolyte solvents (eg. ethylene carbonate EC) on the negative electrode surface and protects it from further reaction with electrolyte. Similarly, but to a lesser extent there is the formation of a cathode-electrolyte interphase (CEI) at the positive electrode. The stability of the formed SEI/CEI determines the electrochemical performance of the cell, the reason why fine-

tuning of SEI/CEI chemistry becomes essential[8]. Such a burden is not specific to Li-ion but common to all battery technologies. The still immature Na-ion battery is not an exception. The reasons are two-fold. First, the early reports show the insufficiency of organic carbonates in protecting the generally used hard carbon negative electrode and the poor stability of formed SEI upon repeated cycling due to higher solubility of the sodium-based SEI components than that of the Li-counterpart[9–11]. Second, alike Li-ion cathodes such as NMC and LiMn$_2$O$_4$, Na-ion cathodes (sodium layered oxides or polyanionic Na$_3$V$_2$(PO$_4$)$_2$F$_3$ (NVPF)), need to be cycled to a similar upper cut-off voltage of 4.4 V and 4.3 V respectively to achieve the maximum capacity out of it. So at such high voltage, electrolyte degradation issues are problematic in both cases. In short, today's Na-ion chemistry suffers from electrolyte degradation at both positive (CEI) and negative (SEI) electrodes that hamper their long cycle life performances. Getting inspiration from the Li-ion technology, the most practical way to address this issue is the inclusion of additional substances, known as electrolyte additives[12], to the main electrolyte for fine-tuning the SEI/CEI chemistry in Na-ion batteries.

The selection of appropriate electrolyte additive(s) requires robust knowledge on the reduction/ oxidation of the additive by itself, its reactivity with other electrolyte components (synergy), possible side reactions, cross-talk between the electrodes and also the nature of products formed. Hence, high throughput techniques are developed where thousands of electrolyte formulations differing by the nature of their components and compositions can be tested to select the best one[13]. In parallel, research efforts have also been directed towards the design of special cells to follow interfacial reactions *operando* condition using techniques such as X-ray photoelectron spectroscopy[14] (XPS), nuclear magnetic resonance[15,16] (NMR), transmission electron microscopy[17] (TEM) etc. Along that line, our group has recently demonstrated the use of optical

sensors that can be placed inside cylindrical/pouch cells as an elegant tool to follow *operando* the heat associated to the chemical reactions during the formation and cycling of the cells [18]. The facile integration of optical sensors with cylindrical/pouch cells helps in exactly mimicking the real-life conditions, hence providing more reliable results.

In the present study, we extend the optical sensing approach to follow indirectly, via heat release, the chemical reactions happening at the electrode-electrolyte interface and the reactivity of electrolyte additives. By combining the knowledge gained from heat generated by different interfacial reactions with parallel electrochemical analyses on NVPF/hard carbon (HC) full cells and NVPF/NVPF, HC/HC symmetric cells, we succeed in grasping the role of different electrolyte additives and their synergy. Based on these observations, we propose an electrolyte formulation having 1M $NaPF_6$ in organic carbonates (ethylene carbonate EC/ propylene carbonate PC/ dimethyl carbonate DMC) as the mother electrolyte with 4 additives namely sodium oxalato(difluoro)borate[19] (NaODFB), vinylene carbonate[20] (VC), succinonitrile[21] (SN) and tris-trimethylsilylphosphite[22] (TMSPi). It shows an optimum electrochemical performance at different cycling temperatures (0, 25 and 55 °C) while having minimum self-discharge. Moreover, we prove the feasibility of transferring the electrolyte to cylindrical 18650 cells, based on the NVPF/HC chemistry that exhibited stable cycling performance at 55 °C, with less gassing.

2. Results and discussions

2.1. Selection of mother/ control electrolyte and the heat evolution during formation cycle

As the starting point, the mother electrolyte has to be properly defined. From some of our previous studies and surveys[23–25], our choice in terms of chemical/electrochemical reactivity and overall performances, narrowed down to 1M $NaPF_6$ dissolved in mixture of ethylene carbonate (EC) - propylene carbonate (PC) - dimethyl carbonate (DMC), with a volume ratio of 1: 1: 1

respectively. EC was chosen because of its key role in the SEI formation[26], DMC the linear carbonate usually incorporated in the electrolyte to reduce its viscosity hence increase the conductivity/wettability[27]. Finally, PC was utilized since it plays an important role in decreasing the freezing point of the electrolyte thus being important for low temperature applications[27–29]. Prior to their use, all the solvents were dried by molecular sieves and tested for their water content by Karl Fischer titration which was less than 5 ppm after drying process. The electrolyte produced by dissolving 1M $NaPF_6$ in a mixture of EC- PC- DMC (1: 1: 1 by volume) exhibit ionic conductivity of 6.07, 11.14 and 15.9 mS cm^{-1} at 0, 25 and 55 °C, respectively. The cycling performance of the electrolyte was then analyzed using coin cells composed of $Na_3V_2(PO_4)_2F_3$ (NVPF) and hard carbon (HC) as positive and negative electrode respectively. The electrode materials (NVPF and HC) used throughout this manuscript are derived from same batches of positive and negative electrode active materials that were coated and calendared in the same way in order to have reliable and meaningful comparisons. The tests were carried out at 55 °C in order for accelerated testing[30]. The cells using the electrolyte formulation 1M $NaPF_6$ in a mixture of EC- PC- DMC exhibited good cycling performance (see Figure S1 in the Supporting Information) and used as mother electrolyte for the rest of this study. The additive-free mother electrolyte is hereafter referred as 'control', in order to differentiate it from the additive-containing electrolyte formulations which are named according to the identity of the involved additives.

The chemical/electrochemical stability of the control electrolyte was tested for its heat evolution during the SEI formation in 18650 NVPF/ HC cells using our recently developed calorimetry technique based on optical sensors[18]. For this purpose, we received electrolyte-free and sealed NVPF/ HC 18650 cells from TIAMAT (France), hence providing freedom to add

multitude of electrolyte combinations while maintaining all the other assembling parameters constants. The cells were pierced to one end with the hole that was used to fill the cell with our electrolyte of choice and also to inject the optical fiber Bragg grating (FBG) sensor prior to be sealed by epoxy. Two other FBG sensors were placed at the cell surface and in its surrounding ambient to perform reliable calorimetry measurements. The cells together with the FBGs were placed in an oven at fixed temperature of 55 °C and formatted following a protocol that consisted of cycling the cell at C/10 rate for 3 charge- discharge cycles. The current and potential of the cells were measured by Bio-Logic potentiostat/ galvanostat and the charge curves for three cycles are shown in **Figure 1a** for the control electrolyte. The FBGs were connected with the optical interrogator to analyze the shift in Bragg wavelength ($\Delta\lambda_B$) that was converted to temperature variations (ΔT) with high resolutions (1 s and 0.1 ^{o}C) as shown in Figure 1b. The ΔT in turn was used to calculate the heat ($\dot{Q}$ in Figure 1c) using a simplified zero-dimensional thermal model whose intrinsic parameters must be defined for each cells prior conducting the measurements (Figure S2, Supporting Information). The heat derivative as a function of voltage was calculated (dQ_{heat}/dV in Figure 1d) and compared with the capacity derivative dQ_{cap}/dV in Figure 1e. From Figure 1d and e, it can be seen that, while very less change in shape is observed in capacity derivative (dQ_{cap}/dV) among the first three charges, a huge change is observed in heat derivatives (dQ_{heat}/dV) where the heat evolution is maximum for the first charge and reduced drastically for the second and third ones. These findings demonstrate the viability of using heat evolution, as determined by FBGs, as a tool to follow the interfacial reactions between electrodes and electrolyte within NPVF/HC cells.

The observed heat changes can be associated with either electrolyte parasitic redox reactions or with electrode material where the phase transitions and diffusion limited kinetics can play a

role[18]. However, since the contributions from electrode materials are expected to be similar on subsequent cycles, the irreversible heat evolutions observed in the first charge are mainly correlated with the electrolyte redox process.
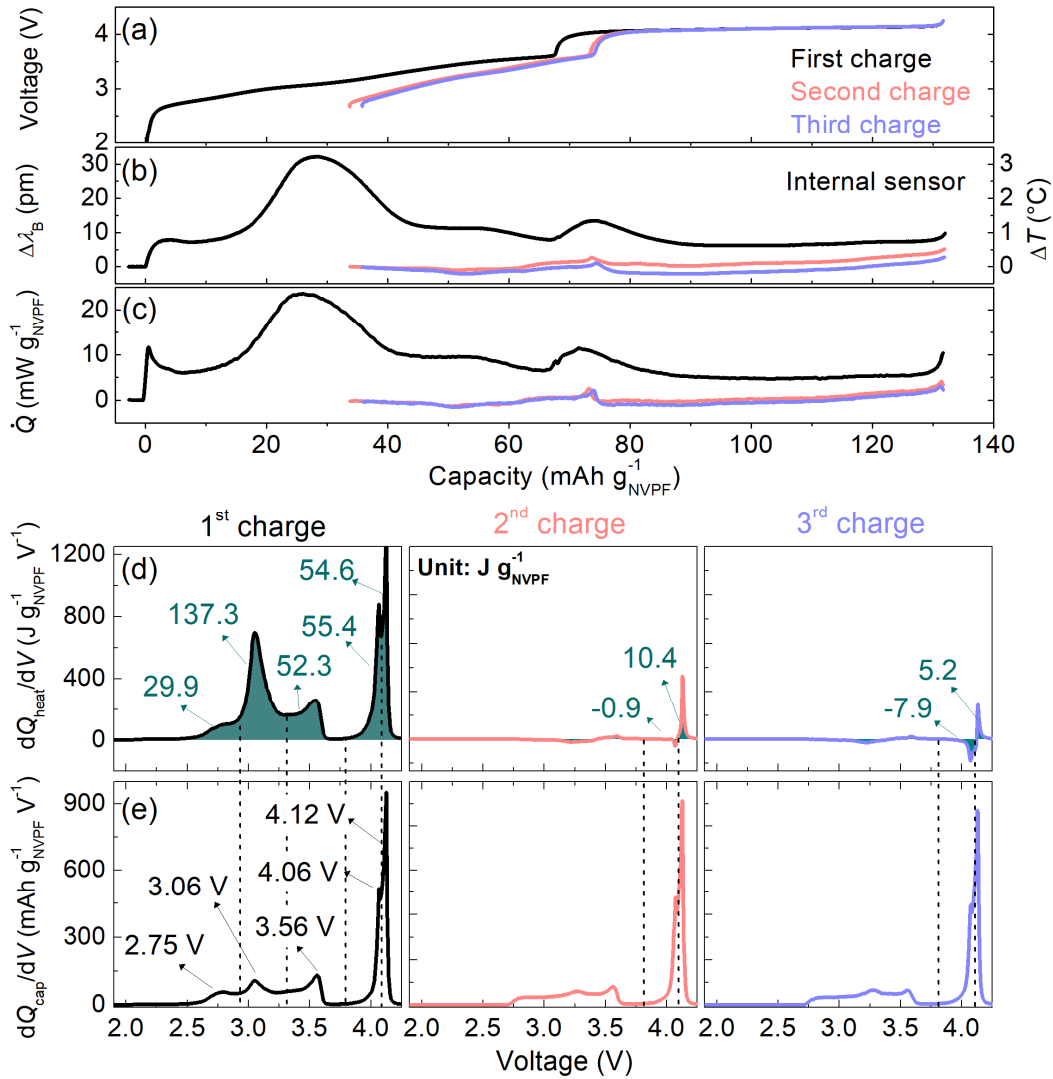
Figure 1. The sensing studies on NVPF/ HC cells using control electrolyte. (a) The capacity vs voltage plot (b) The change in Bragg wavelength ($\Delta\lambda_B$) measured by FBGs and converted to the equivalent temperature change (ΔT) in the right y-axis as a function of capacity. (c) The heat $\dot{Q}$ as a function of capacity. (d) Derivative of heat evolution (dQ_{heat}/dV), mentioned values indicate integrated heat in J/g_{NVPF} for regions separated by dashed line and (e) Derivative of capacity (dQ_{cap}/dV) as a function of cell voltage for the 1st, 2nd, and 3rd charges, voltage values corresponding to the peaks are labelled in the

figure. The experiment was duplicated using two cells with exact configuration and identical results were observed in both cells. The cells were cycled at 55 °C from 2 to 4.25 V at C/10 rate (1C = 128 mAh g^{-1}).

By comparing the potential of the NVPF and HC individual electrodes (see Figure S3 in the Supporting Information), the region from OCV to 3.8 V corresponds to the slopy region of hard carbon, hence the observed exothermic peaks at 2.75, 3.06 and 3.56 V (Figure 1e) are correlated with the SEI formation which stabilized after the first cycle. In contrast, the other two exothermic peaks (4.06 and 4.12 V) occurring beyond 50 % of the cell charging capacity happens in the high voltage plateau of NVPF hence includes heat of reaction related to $Na_2V_2(PO_4)_2F_3$-$NaV_2(PO_4)_2F_3$ phase transition as well as diffusion limited kinetics, in addition to the possible electrolyte oxidation. The process at 4.06 V becomes endothermic on 2nd and 3rd charges indicating the exothermic heat observed in 1st charge is mainly from electrolyte oxidation. However, only a decrease in exothermicity is observed for the process at 4.12 V in moving from 1st to 2nd and 3rd charges, hence it is correlated with electrolyte oxidation as well the diffusion limited kinetics at the end of charge from material[18].

2.2. Understanding the role of electrolyte additives by sensing

Next, we studied how the heat events occurring through the charging process are evolving upon the addition of various chemical additives. For this purpose, the additives selected from sodium oxalato(difluoro)borate (NaODFB), vinylene carbonate (VC), succinonitrile (SN) and tristrimethylsilylphophite (TMSPi) were added to the mother electrolyte, consecutively in a defined ratio, starting from 0.5 wt % NaODFB, 3 wt % VC, 3 wt % SN and 0.2 wt % TMSPi. All these additives were selected as they are widely in-use for LIBs and also understudy for NIBs as reported earlier[19,24,25]. For each electrolyte formulation, the measurements were done at least

twice to ensure the reproducibility of the results. In total, 5 different electrolyte formulations namely control, NaODFB, NaODFB+ VC, NaODFB+ VC+SN and NaODFB+ VC+ SN+ TMSPi were studied and the cycling curves with their corresponding dQ_{cap}/dV plots are shown in Figures S4 and S5 in the Supporting Information.
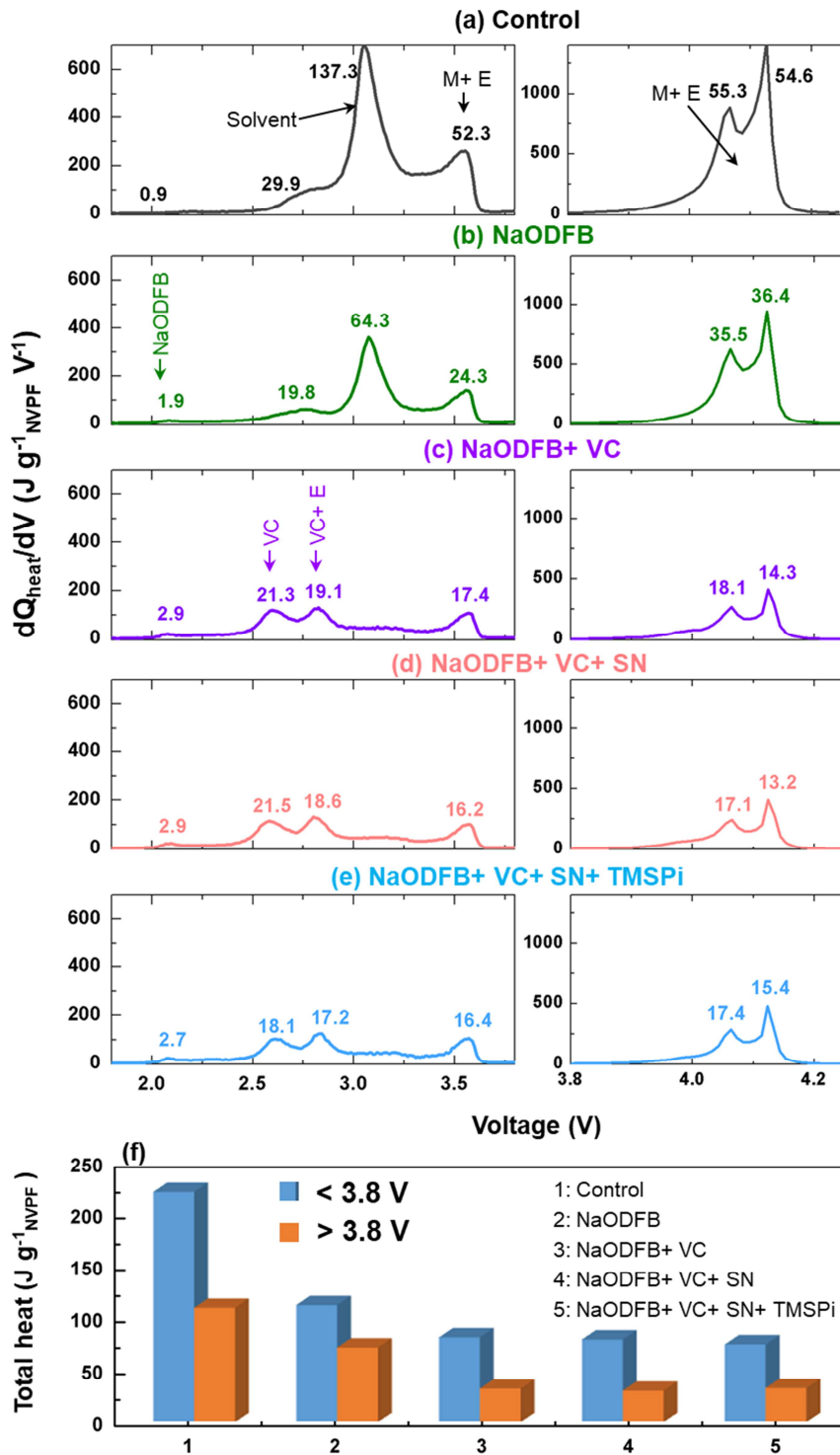
The ΔT measured from FBG's is used to derive the dQ$_{heat}$/dV derivative plots as explained for the control and the data for 1st charge are shown in **Figure 2 (a-e)** with that of 2nd and 3rd charges in Figure S6 of Supporting Information. For the sake of clarity, we plotted the data in two panels that reunite the heat events occurring below 3.8 V (left) and those above (right) to decouple the impacts of the additive on the HC and NVPF electrodes respectively. Note that the onset potential of the new thermal events compared to the control electrolyte together with their amplitudes is a function of the additive used. The total evolved heat in both of these voltage regions (< 3.8 V and > 3.8 V) for each electrolyte formulation is plotted in Figure 2f (bottom panel). Strikingly, there is an abrupt decrease in the cumulated heat in the two voltage regions with the addition of electrolyte additive(s) (Figure 2f) implying the additives assist the formation of SEI and CEI that reduce the unwanted parasitic reactions with the electrolyte solvents.

Nearly 50 % reduction in evolved heat is observed just by the addition of the single additive NaODFB (Figure 2b) demonstrating the reactivity of NaODFB or its derived product in both negative and positive electrodes. The heat due to NaODFB reduction at ~2 V is much less, around 2 J/g$_{NVPF}$, implying its effectiveness in protecting the electrode surface without actually releasing unwanted heat. Still, the peaks owing to solvent reduction at 2.75, 3.06 and 3.56 V persist suggesting that solely NaODFB is not sufficient in stopping excessive solvent reduction. When VC was added together with NaODFB (Figure 2c), a nearly complete reduction in heat associated with solvent reduction at 3 V is observed. The heat profile consists of 2 new

9

exothermic processes at 2.6 V and 2.8 V, where the 2.8 V process overlaps with the solvent reduction observed in the control electrolyte (2.75 V). The peak at 2.6 V corresponds to 1.0 V in hard carbon vs Na^+/ Na^0 (Figure S3) that matches closely with the 1.4 V vs Li^+/Li^0 reported for vinylene carbonate reduction[31]. Further, a closer comparison using dQ_{cap}/dV with dQ_{heat}/dV plot (Figure S7, Supporting Information) showed that both 2.6 and 2.8 V redox process exhibit nearly similar heat evolution (21 and 19 J per gram of NVPF), however solely 0.065 electron (0.065 Na^+ removal from NVPF) is involved at 2.6 V reduction versus 0.22 electron at 2.8 V reduction. The result indicates the VC reduction at 2.6 V is either highly exothermic or associated with parallel chemical reaction that evolves huge amount of heat. It correlates well with the VC redox mechanism reported in literature where VC involves a 1 or 2 electron redox process[32–34] (exothermic peak at 2.6 V) with the products of VC reduction that in turn reacts with EC (peak at 2.8 V) and polymerize with the release of CO_2. The evolved heat at 2.6 V is relatively higher when VC is used alone (see Figure S8 in the Supporting Information) without NaODFB as the available HC surface is higher without passivation by NaODFB. In the high voltage region (3.8-4.25 V), the addition of VC reduced the overall heat and relatively less changes in heat of reaction are observed in the second and third charges (see Figure S6 in the Supporting Information) indicating possible passivation and stabilization of positive electrode as well.

The additive succinonitrile (SN) was tested next as it was reported to be efficient in protecting the positive electrode[21,35–37]. The addition of SN to NaODFB+ VC further reduced the heat associated with high-voltage region (> 3.8 V) process indicating a relatively less severe electrolyte oxidation in the positive electrode, hence suggesting a synergetic effect[37] of SN together with VC to protect the positive electrode efficiently (Figure 2d). However, we do not see

any new specific feature pertaining to the addition of SN that could suggest its oxidation or adsorption on electrode surface.

(a) Control

(b) NaODFB

(c) NaODFB+ VC

(d) NaODFB+ VC+ SN

(e) NaODFB+ VC+ SN+ TMSPi

Voltage (V)

(f)

1: Control
2: NaODFB
3: NaODFB+ VC
4: NaODFB+ VC+ SN
5: NaODFB+ VC+ SN+ TMSPi

Figure 2. (a-e) The derivatives of heat with respect to voltage (dQ_{heat}/dV) of NVPF/HC cylindrical 18650 cells cycled at C/10 in an oven maintained at 55 °C, using 1M NaPF$_6$ in 1: 1: 1 (by volume) of EC: PC: DMC electrolyte with (a) no additives- control, and with the additives (b) 0.5 wt% NaODFB, (c) 0.5 wt% NaODFB+ 3 wt% VC, (d) 0.5 wt% NaODFB+ 3 wt% VC+ 3 wt% SN, and (e) 0.5 wt% NaODFB+ 3 wt% VC+ 3 wt% SN+ 0.2 wt% TMSPi. The figures in the left show the voltage window from OCV-3.8 V and the right ones show the voltage window from 3.8 to 4.25 V. The integrated heats (in joule per gram of NVPF) of SEI/CEI formation peaks were labelled and the arrow marks are guide to eyes to show the redox process of NaODFB, VC, electrolyte solvent (E) and heat evolution due to sodium (de-)insertion in the material (M). (f) The total heat observed at < 3.8 V and >3.8 V as a function of electrolyte formulation.

Similarly, addition of TMSPi (0.2 wt %) also did not show any new feature in the heat derivative plot, with the exception of a reduction of the evolved heat in the low voltage processes (< 3.8 V; Figure 2e). It is known from literature that TMSPi is an effective acid/O$_2$ scavenger[22,38,39] and this could be responsible for the reduced heat in the low voltage process. On the contrary, a slight increase in heat is observed at high voltages that we are associating to the oxidation of TMSPi (calculated oxidation potential[39] is 4.29 V vs Li$^+$/Li^0) or one of its reduction products in the positive electrode.

Altogether, these calorimetry measurements indicated a reactivity of the studied electrolyte additives both at the NVPF and HC electrodes with the exception of SN that solely showed an activity on the NVPF electrode. Moreover, the additive mixture of NaODFB with VC participate in the formation of both SEI and CEI, whereas SN, TMSPi may be helpful to fine-tune them further as they exhibited further reduction in heat of reaction since the smallest heat was obtained when the four additives altogether were added to our mother electrolyte. Such a finding provided a very useful guidance but not sufficient in deriving the best suitable electrolyte for the NVPF/HC chemistry. Hence, we substantiated our studies by electrochemical analyses using the same combinations of additive blends in NVPF/HC Na-ion full cells.

2.3. Electrochemical analyses in Na-ion full cells:

Coin-type 2032 cells were assembled and cycled at 55 °C between 2 - 4.3 V according to the following experimental protocol. For data robustness, a minimum of 2 coin cells were assembled with each electrolyte formulations and the cells were initially cycled at C/5 rate for 10 times to form the stable SEI/ CEI prior applying a self-discharge test by keeping the cells at rest on 100 % state of charge (4.3 V) for 1 week at 55 °C. After the self-discharge test, the cycling was resumed and the capacity recovered after the self-discharge period (Q_n) was used to calculate the loss due to self-discharge ($Q_{n-1}-Q_n$). The capacity of the subsequent cycle (Q_{n+1}) is the recovered capacity. For clarity, the cycling curves for n-1, n and n+1th cycles alone for all electrolyte formulations are shown in Figure 3(a-d) with the complete cycling data in Figure S9 of the Supporting Information. The addition of electrolyte additives improves the stability during self-discharge test, and all the electrolytes with additives showed only a 9-10 % of capacity loss during 1 week rest at 55 °C, while the control electrolyte exhibits 16 % loss with solely 90 % recovery (Figure 3e).

An increase in polarization is observed with all electrolyte formulations after the self-discharge test. The polarization is calculated as the difference in average cell voltage between charge and discharge and mentioned in figure 3a-d. The electrolytes with NaODFB+ VC and NaODFB+ VC+ SN+ TMSPi showed the least change in polarization (ΔV_{n+1}- ΔV_{n-1}= ~20 mV) in line with the best capacity recovery of 94.7 and 96.6 % respectively. A relatively higher increase in polarization (~50 mV) is observed with NaODFB+ VC + SN and the highest with control electrolyte (~100 mV). The results show possible SEI/ CEI growth due to side reactions during rest hence increased impedance.
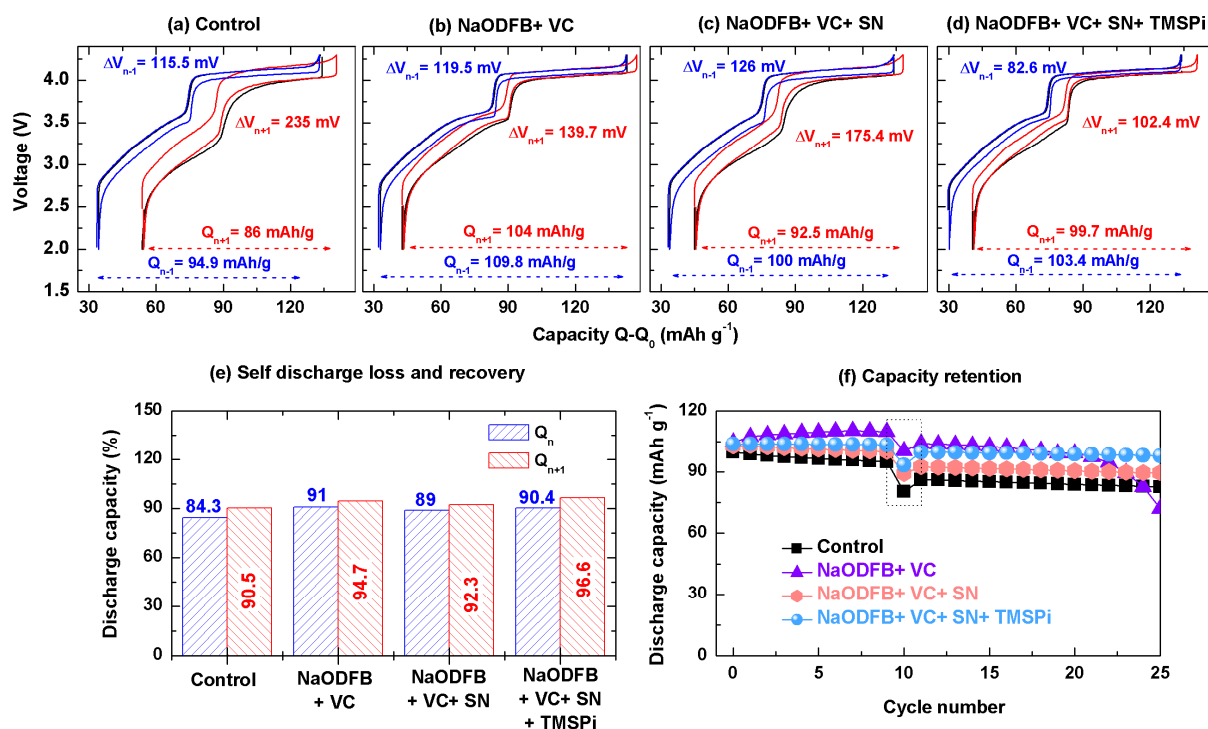
Figure 3. a-d) Cycling curves of NVPF/HC cells (derived from Figure S9 of the Supporting Information) using 4 different electrolyte formulations, where only the cycle corresponds to self-discharge test and the recovery cycle are shown. Q_n and Q_{n+1} represent the capacity after self-discharge and the recovered capacity in subsequent cycle. (e) discharge capacity during self-discharge and recovery cycle and (f) Capacity retention of the cells using control electrolyte, and with the additives 0.5 wt% NaODFB, 0.5 wt% NaODFB+ 3 wt% VC, 0.5 wt% NaODFB+ 3 wt% VC+ 3 wt% SN, and 0.5 wt% NaODFB+ 3 wt% VC+ 3 wt% SN+ 0.2 wt% TMSPi.

The capacity retentions of all the cells before and after the self-discharge test are shown in Figure 3e. A stable capacity retention with slightly reduced capacity after self-discharge is observed with all electrolyte formulations except NaODFB+ VC that showed initial increase in capacity and sudden drop after 15-20 cycles. Notably, the NaODFB+ VC exhibit less self-discharge loss (~9 %) and only ~20 mV increase in polarization after self-discharge tests. In this case, the observed deterioration is unexpected and we tried to understand it further via a dV/dQ analyses[40,41] of the full cells. It can be expressed as $dV_{cell}/dQ = (dV_{cathode}/dQ) - (dV_{anode}/dQ)$, hence enabling the feasibility to distinguish the degradation contribution from positive and negative electrodes separately without inserting a reference electrode.

14

In the previous work[42] from our group, we have shown that such analysis becomes extremely simple for the NVPF/HC system which shows a single and well defined peak between the two plateaus ($Na_3V_2(PO_4)_2F_3$ → $Na_2V_2(PO_4)_2F_3$ and $Na_2V_2(PO_4)_2F_3$ → $Na_1V_2(PO_4)_2F_3$) with the derivative shooting to infinite at the very beginning and at the end of charge-discharge, respectively. Briefly, the shift of the peak (NVPF slippage) and the shoot (HC slippage) shown in Figure 4a are indicative of the NVPF and HC degradation, respectively. Figure 4 shows the variations of the dV_{cell}/dQ analysis for the 1st, 10th and 20th discharge cycles for the control electrolyte and the derived ones containing different additives. From these dV_{cell}/dQ plots we directly visualized the beneficial effects of the four additives with barely any change at the positive electrode. For better comparison, we plotted the variation of the NVPF and HC slippages for various electrolytes in Figure 4b and the least slippage of both electrodes is obtained for the four additive components electrolytes.

However, worth mentioning is the case of VC + NaODFB which initially showed a shift of the NVPF and HC to opposite (negative) directions than for the other electrolytes prior to follow the similar trend after the 10th cycle. It means that, in this case we have the oxidation of the electrolyte with simultaneous insertion of Na^+ in the HC, leading to higher capacity hence negative slippage on both NVPF and HC.
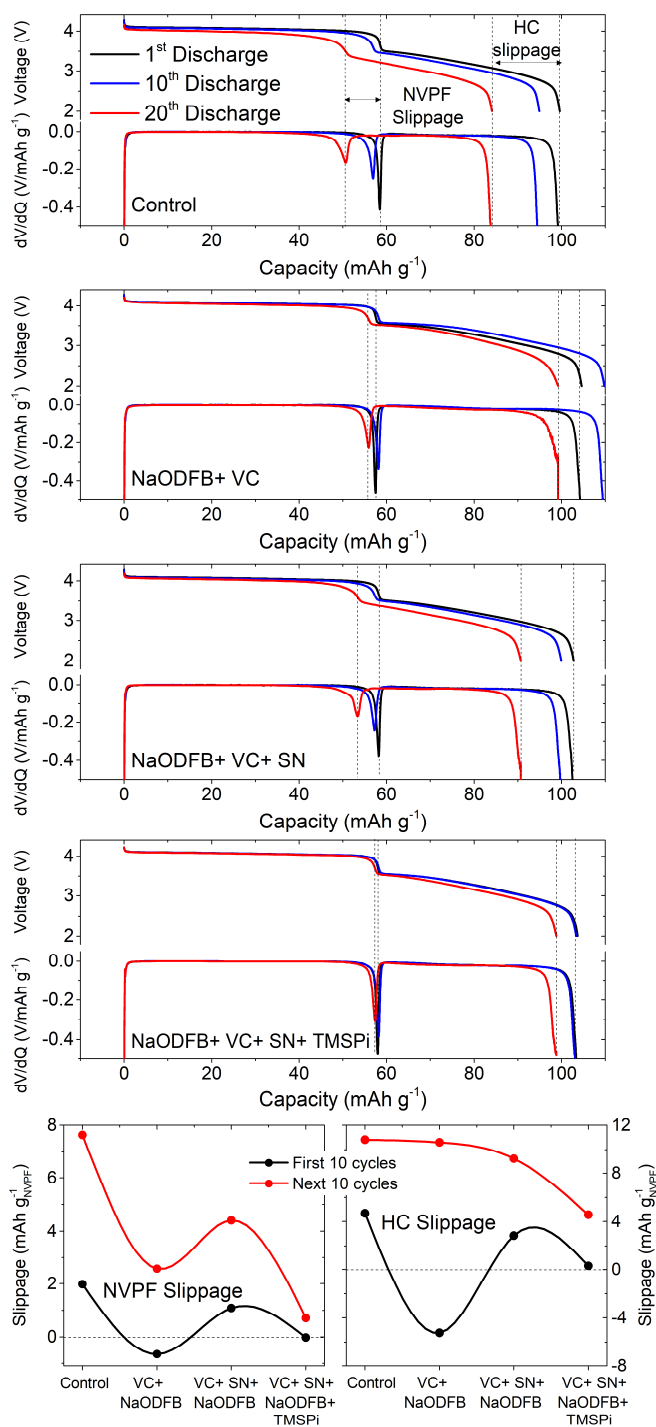
**Figure 4.** (a) The discharge voltage versus capacity plots of the 1st, 10th and 20th cycles together with differential voltage (dV/dQ) for the cells with control electrolyte, and with the additives 0.5 wt% NaODFB, 0.5 wt% NaODFB+ 3 wt% VC, 0.5 wt% NaODFB+ 3 wt% VC+ 3 wt% SN, and 0.5 wt% NaODFB+ 3 wt% VC+ 3 wt% SN+ 0.2 wt% TMSPi. The curves are derived from NVPF/HC cells for which the original data is shown in Figure S9 of the Supporting Information. (b) The capacity slippage in positive (NVPF) and negative (HC) electrodes calculated from (a).

The poor oxidative stability of NaODFB+ VC is re-confirmed from more pronounced end-point slippage in charge than in discharge (see Figure S10 in the Supporting Information). Charge endpoint slippage and Discharge endpoint slippage values gives indication about electrolyte oxidation and Na^+ inventory loss for the SEI growth, respectively[43,44]. Yet, it must be realized that all these analyses in NVPF/HC full cells include cross-talk (e.g., shuttle) between oxidation and reduction parasitic species formed at the positive and negative electrode, respectively. Therefore separating this cross-talk and identifying the electrolyte stability against a single mode of degradation becomes essential.

To interrogate the cross-talking between electrodes, we followed Jeff Dahn's approach of symmetric cells cycling[45–47]. Cells using desodiated $Na_1V_2(PO_4)_2F_3$ | sodiated $Na{\sim}_3V_2(PO_4)_2F_3$ and desodiated hard carbon | sodiated hard carbon, respectively were assembled with electrodes prepared and recovered according to the protocol described in experimental section. The representative cycling curves and individual electrode curves calculated with dV/dQ fitting software[41] are presented in Figure S11 and Note S1 of the Supporting Information. The changes in the cycling curves are associated with the degradation mode and shown in Figure S12 and Note S2-S3 of the Supporting Information. It is worth noting that dominant mechanism for degradation of NVPF and HC symmetric cell is electrolyte oxidation and electrolyte reduction, respectively. The cumulated capacity retention plots of both NVPF and HC symmetric cells are shown in Figure 5.

For NVPF symmetric cells, the least capacity retention is observed for the control and VC+ NaODFB additive combination (Figure 5a) and the capacity decay is well pronounced starting from initial cycles. This implies that the observed deterioration in full cells (Figure 3f) mainly comes from poor oxidative stability of electrolyte as deduced earlier from the slippage calculations. However, the electrolyte stability improved drastically by the addition of SN that

protects the NVPF electrode and improves the oxidative stability of the electrolyte. Addition of TMSPi to NaODFB+ VC+ SN did not bring any significant change in the stability, while similar performance to that of NaODFB+ VC+ SN without TMSPi is observed.
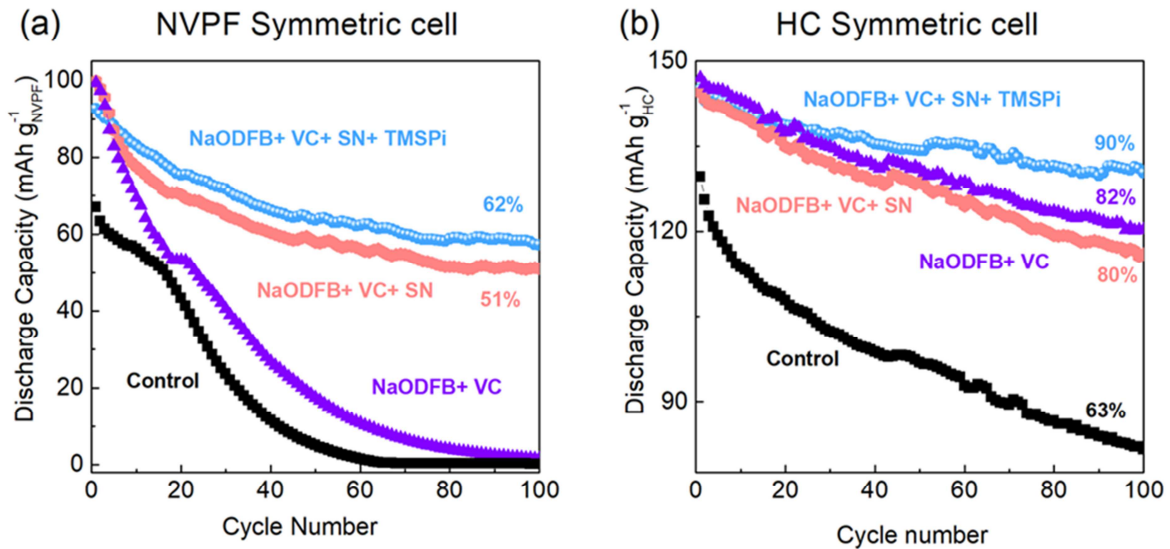

Figure 5. Discharge capacity as a function of cycle number for the cells using control electrolyte, and with the additives 0.5 wt% NaODFB, 0.5 wt% NaODFB+ 3 wt% VC, 0.5 wt% NaODFB+ 3 wt% VC+ 3 wt% SN, and 0.5 wt% NaODFB+ 3 wt% VC+ 3 wt% SN+ 0.2 wt% TMSPi in (a) NVPF and (b) HC symmetric cells cycled at 25°C with C/5 rate.

Turning to hard carbon symmetric cells, surprisingly, the degradation is not as dependent as for NVPF cells (Figure 5b). With inclusion of additives nearly 80-90 % of the initial capacity is retained even after 100 cycles in HC symmetric cells as compared to 50 to 60% for the NVPF cells. A stable performance is observed with NaODFB+ VC additives itself and betterment in stability is obtained with NaODFB+ VC+ SN+ TMSPi. The stability in HC symmetric cell cycling indicates the good SEI which prevents further electrolyte reduction and SEI growth. Altogether, the observed degradation with NaODFB+ VC is sufficient in creating good SEI but still NVPF/HC full cell shows capacity decay due to poor oxidative stability of the electrolyte. Addition of SN protects the NVPF surface hence reduce electrolyte oxidation. The additive

TMSPi helps in further improving the SEI stability hence the electrolyte with NaODFB+ VC+ SN+ TMSPi shows the best stability with respect to both SEI and CEI.

2.4. Practicality of the proposed electrolyte:

For the sake of completion, we discuss next the practicality of the electrolyte formulation with additives NaODFB+ VC+ SN+ TMSPi that show the best optimized performance overall. First, the ionic conductivity is measured and the values obtained are slightly lower than the control electrolyte, 5.9, 10.49 and 15.8 mS cm^{-1} at 0, 25 and 55 °C respectively. Cycling experiments were then conducted in 2032 coin cells at 0, 25 and 55 °C (Figure 6a-c). Whatever the temperature, the electrolyte showed good electrochemical performance with only 3% capacity loss and 100% recovery (Figure 6d) at both 0 and 25°C, after self-discharge tests for 1 week at 100% SOC (4.3 V, after the removal of 2 Na from NVPF). When raising the temperature to 55 °C the cells showed nearly 10% capacity loss during rest for 1 week with the recovery of 96% capacity. The capacity retention plots in Figure 6e shows stable capacity retention before and after self-discharge. In order to validate the knowledge transfer from coin cells to prototype cylindrical cells, we also assembled 18650 cells using our proposed electrolyte. The cells are initially formatted at 55 °C by charging at C/10 rate for one charge (4.3 V) and then allowed for cycling at C/5 for 10 cycles followed by self-discharge test for 1 week and recovery cycles using same rate. The experiments are conducted at both 25 °C (Figure 6f) and 55 °C (Figure 6g) and similar results as that of coin cells were obtained with 18650 cells. The cell exhibited ~98 % capacity recovery even at 55 °C after 1 week rest at full SOC (4.3 V). The long cycling performance was tested at 1C rate and are shown in Figure 6f and g.
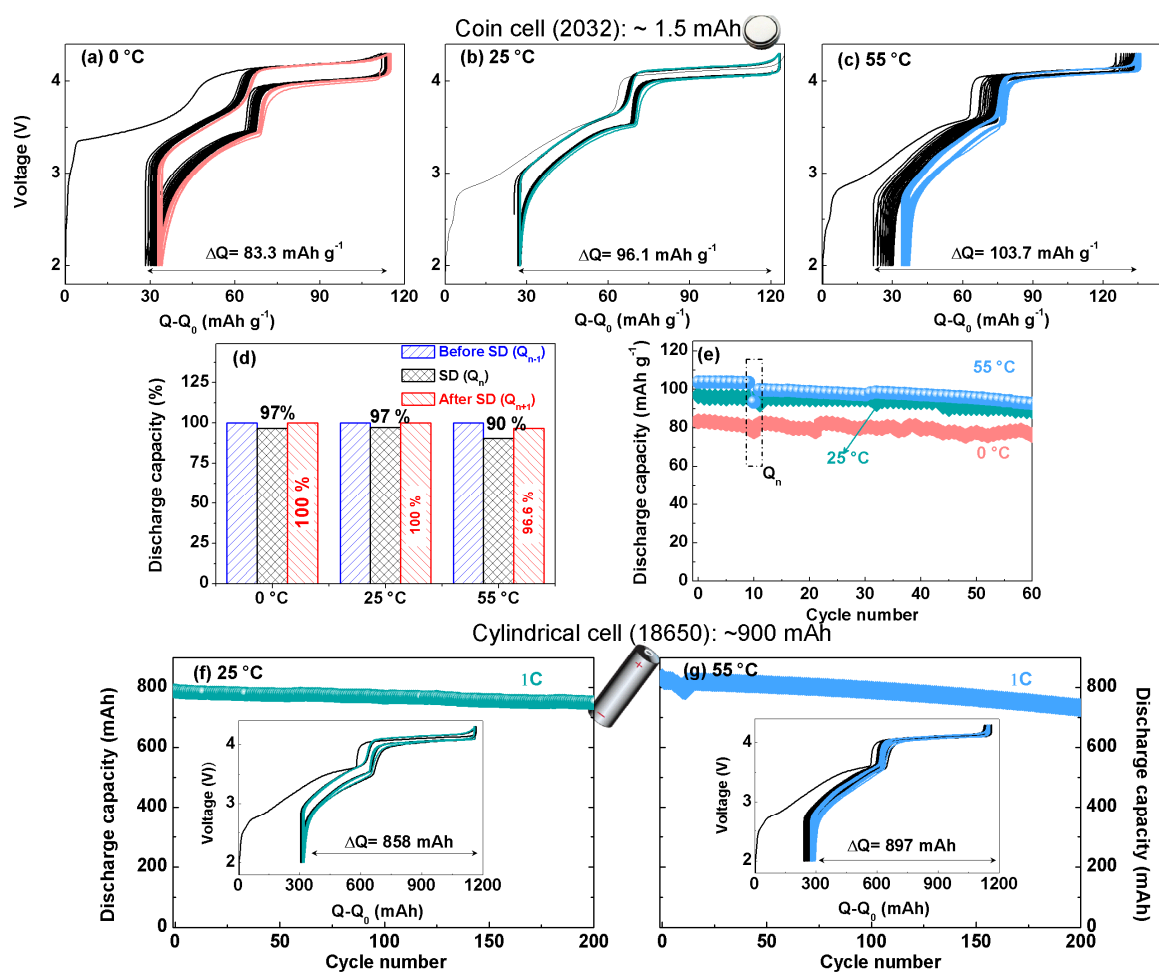
Figure 6. Electrochemical performance of NVPF/HC cells using the electrolyte 1M $NaPF_6$ in 1: 1: 1 EC: PC: DMC containing 0.5 wt% NaODFB, 3 wt% VC, 3 wt% SN and 0.2 wt % TMSPi additives. (a- e) Data derived by testing in coin type 2032 cells; the cells are cycled at constant at temperatures of (a) 0 , (b) 25 and (c) 55 °C. (d) The comparison of discharge capacity observed before self-discharge test (Q_{n-1}), in self-discharge cycle (Q_n) and after self-discharge test (Q_{n+1}). (e) Capacity retention plot where the 10th cycle capacity is due to self-discharge test. (f and g) Data derived from 18650 cells; Capacity retention at 1C of the cells cycled at (a) 25 °C, (b) 55 °C; the data are derived after the self-discharge test where the cells were cycled minimum 20 cycles and also allowed to rest for 1 week at 100% SOC. The inset in each plot show the cycling profile for formation cycle (black) and after self-discharge test (green for 25 °C and blue for 55 °C) in which the cells were cycled at C/5 rate.

Another figure of merit for practical application is safety of the battery together with its gassing that should remain minimum. This issue is more acute here, as VC and in few studies TMSPi were reported to be leading to gassing in Li-ion batteries[48,49]. To evaluate gassing, we carried out online electrochemical mass spectrometry (OEMS) studies in which specially designed cells

were assembled using NVPF and HC electrodes. Two different electrolytes were studied, where the first one consists of 1 M $NaPF_6$ in EC: PC: DMC and additives 0.5 wt% NaODFB + 3 wt% VC + 3 wt% SN without TMSPi, and a second one having the same composition but with 0.2 wt % TMSPi. The cells were cycled at 55 °C using C/10 rate and the evolved gases during cycling were analyzed using mass spectrometer in which signals corresponding to CO_2, H_2 and C_2H_4 gases were calibrated. The POF_3 and trimethylfluorosilane (TMSF) gases, which are reported as side-products from $NaPF_6$ decomposition and TMSPi reaction with fluoride ion, respectively, were also recorded but not quantified.

The results are compiled in Figure 7a .small amount of POF_3 and TMSF were spotted only for electrolyte containing TMSPi in the first cycle, in agreement with literatures where the TMSPi is reported to induce PF_6^- decomposition[49]. In addition, we note similar amount of C_2H_4 gas produced, irrespective of the presence or absence of TMSPi in the electrolyte. This is in line with limited EC reduction as the SEI is mainly formed from the reduction of NaODFB and VC. However, the NVPF/HC cell containing the electrolyte with NaODFB+ VC+ SN is associated with huge evolution of CO_2 gas during SEI formation (< 3.8 V). The amount of released CO_2 is reduced nearly by five-fold with the addition of TMSPi. On the other hand, the H_2 amount is not significantly affected by the presence of TMSPi, suggesting a separate process that is most probably related to reduction of protic species on the anode[50]. Overall, though TMSPi leads to small amount of POF_3 and TMSF gases in the first cycle, it helps to drastically reduce the CO_2 amount, which is likely caused by synergetic effects between TMSPi and the rest of the electrolyte additives.

The aforementioned gassing results are quite surprising as we observed huge gassing while using the electrolyte containing NaODFB+ VC+ TMSPi additives reported from our group

previously[24]. Worth to mention, such vigorous gassing was observed mainly in 18650 cells where the used active material amount was much higher than the coin type or OEMS cells (~20 mg of NVPF for OEMS cells vs 9 g for 18650 cells) and when the cells were cycled at 55 °C for long cycling. Due to difficulties in performing long-term cycling of the OEMS cells, we have used once again optical sensors to follow the pressure evolution upon long cycling. For this purpose, the 18650 cells were integrated with microstructured optical fiber (MOF-FBG) that is sensitive to hydraulic pressure in addition with single mode optical fibers (SMF- FBG) that are poorly sensitive to pressure changes.

The results were compared together in order to calculate the pressure changes (see experimental methods) upon cycling. The data in Figure 7b compares the change in pressure as a function of cycle number for two different electrolyte formulations, namely NaODFB+ VC+ TMSPi that is similar to our previous report[23] and NaODFB+ VC+ SN+ TMSPi discussed in this manuscript. The cells without SN (NaODFB+ VC+ TMSPi) exhibited gradual increase in cell pressure and lead to CID break when the pressure reaches the maximum limit of ~16 bars inside the cell. In contrast, the electrolyte containing SN in its formulation (NaODFB+ VC+ SN+ TMSPi) showed much less change in pressure re-confirming the low amount of gassing observed with this electrolyte formulation. The main difference between the two studied electrolytes in Figure 7b is the presence or absence of SN. It is known from the symmetric cells studies (Figure 5a) that SN protects the positive electrode. It indicates that the huge gassing observed in absence of SN comes from electrolyte oxidation leading to in-built pressure increase and deterioration in cell performance.
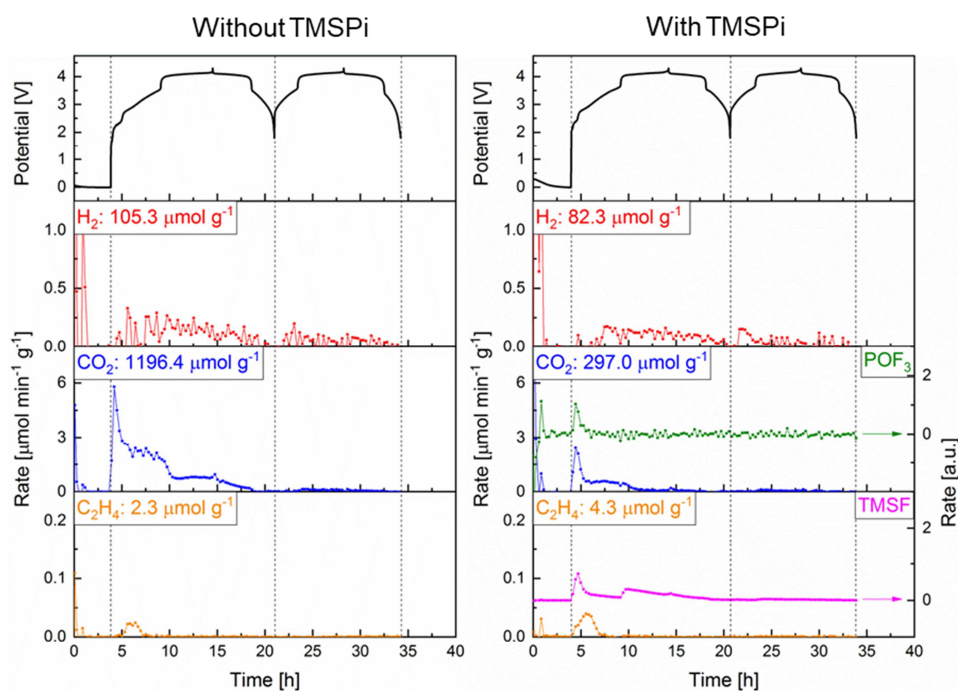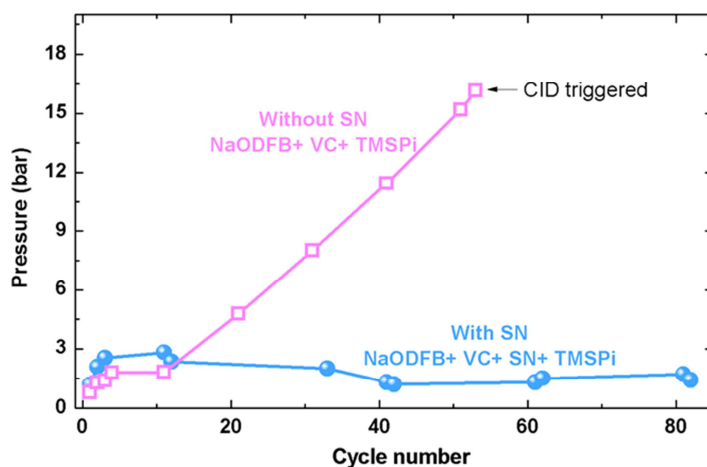
Figure 7. (a) OEMS analyses of the NVPF/HC cells using 1M $NaPF_6$ in EC: PC: DMC and electrolyte additives NaODFB+ VC+ SN without (left) and with (right) TMSPi added to the electrolyte. The numbers in each panel represent the total amount of H_2, CO_2 and C_2H_4 gases evolved from the cell during cycling. The gases POF_3 and TMSF were observed only when TMSPi was used in the electrolyte and were not quantified. (b) The change in cell pressure (followed by FBGs) of the NVPF/ HC cylindrical 18650 cells upon cycling at 55 °C using C/10 rate. The electrolyte consist of 1M $NaPF_6$ in 1: 1: 1 EC: PC: DMC where the additives used are NaODFB+ VC+ TMSPi with (blue circles) and without SN (pink squares).

3. Conclusion

Altogether, the electrolyte 1M $NaPF_6$ in EC: PC: DMC consisting of the studied 4 electrolyte additives 0.5 wt % NaODFB, 3 wt % VC, 3 wt % SN and 0.2 wt % TMSPi conjointly exhibited a stable SEI/ CEI formation that reflected in their electrochemical performance. The symmetric cell studies showed that the electrolyte with no additive deteriorates quite fast and the effect is more prominent in the NVPF electrode. The pronounced electrolyte oxidation together with SEI/CEI dissolution and loss in Na^+ inventory lead to faster self-discharge during rest. Consequently, the usage of electrolyte additives to stabilize both CEI and SEI becomes essential.

At present, the trial and error method has been the choice of researchers to come up with best electrolyte combinations. Though it is very useful, it calls for vast amount of experiments in order to achieve effective comparison. Further, translating the knowledge obtained from one material to others is not feasible without the deeper understanding of the role of electrolyte additives. Different post-mortem analyses techniques are in use to identify the nature of formed interphases and postulate the possible interfacial reactions. However, *operando* techniques are expected to provide more direct information.

The sensing analyses to follow the heat evolutions during cycling seems to be a viable technique to understand the interfacial reactions as most of the electrolyte redox processes are exothermic. The information obtained helps to screen the additives depending on the requirement. The ideal case will be to study the additive reactivity as a function of its stoichiometry, C-rate and temperature to determine the reaction kinetics which in turn can be an input data file to predict the interfacial reactions. At present, theoretical calculations are available to predict redox potential and energy of the different electrolyte additives. However, the prediction becomes complex when many additives that can work in synergy have to be used together. In such case,

we believe that the heat evolutions measured from sensing experiments together with their redox potential can serve as an information source for predicting the exact interfacial reactions. By coupling the temperature studies with pressure analysis which is feasible using specially designed sensors we could provide much more information about the associated gassing and pressure increase.

In short, we have identified a new electrolyte composition for achieving highly performing 18650 Na-ion cells based on the NVPF/HC chemistry via *operando* optical calorimetry combined to an arsenal of electrochemical tests and OEMS measurements. This provides an attractive methodology to design efficient electrolytes for specific electrodes and we hope that the battery community will from now on consider such a new sensing tool to interrogate interphase formation and other the cascade reactions in battery chemistries beyond Na or Li-ion.

4. Experimental Procedure

Electrolyte Preparation: All the electrolytes were prepared by dissolving one molar $NaPF_6$ (Stella, Japan) in battery grade solvents (DoDochem, China) in the Ar-filled glovebox (MBraun MB200B). The solvent mixture EC- PC- DMC in 1: 1: 1 volume ratio was dried by molecular sieves (4 Å, Sigma-Aldrich) till its water content lower than 5 ppm, confirmed by Karl-Fisher titration (Metrohm 899 coulometer). The additive NaODFB is prepared in-house as reported earlier and other additives Vinylene carbonate (TCI, Europe), Succinonitrile (Acros Organics), and Tris(trimethylsilyl) Phosphite (TCI, Europe) were purchased and used as such, except succinonitrile which is melted at 70 °C and weighed in liquid state.

Ionic conductivity Measurement: Bulk ionic conductivity of the electrolyte solutions were measured using a Mettler Toledo S230 conductivity meter. Before the measurement, the conductivity probe was calibrated using a standard solution of conductivity 12.88 mS.cm^{-1} at 25 °C. 3 mL of the electrolyte was taken in a brown glass vial and was then placed in a temperature-controlled bath. Conductivity was measured at 0°C, 25°C and 55°C. At each temperature step, a

constant temperature was maintained for at least 20min to allow the electrolyte temperature to equilibrate with the bath temperature.

Electrochemical testing of NVPF/HC coin cells: $Na_3V_2(PO_4)_2F_3$ and hard carbon coated on Al foil were received from Tiamat, France. The electrodes were specially coated only on one side of the Al foil for conducting the studies in coin cells, however they are designed to have exact mass loading as in cylindrical 18650 cells. The electrode thickness, active material to conducting carbon and binder ratio, porosity etc were maintained the same as in 18650 cells. All of the electrodes were dried in a Buchi oven under vacuum (lower than 100 mbar) at 80° C for 12 h prior to being transferred into the glovebox. The electrochemical performance of NVPF/HC full cells were evaluated in 2032- type coin cells separated by two layers of glass fiber containing 150 µL of desired electrolytes. All cells were galvanostatically cycled by using MPG2 potentisostat or BCS battery cycler (Bio-Logic, France) at 55 °C, and the cycling rates were calculated with respect to NVPF (1C = 128 mA g^{-1}).

Sensing and Electrochemical testing of NVPF/HC cylindrical 18650 cells: Hermetically sealed NVPF/HC cylindrical 18650 cells without electrolyte were received from Tiamat, France. A 0.8 mm diameter hole was drilled into the negative pole of the dry, 18650 cells. The position was selected according to the welding point of the negative current collector, which was close to the center of the negative pole. This choice of the position helped in avoiding destruction of the jelly roll and in preventing the strain interaction between the FBG sensors and the jelly roll. All of the 18650 cells were dried in Buchi oven under vacuum at 80 °C for 12 h prior to being transferred into the glovebox. The 18650 cells were then filled with 5.5 mL of desired electrolyte inside the glovebox. Then the FBG sensors were inserted into the central void of the jelly roll through the drilled hole using a needle. The interface between the needle containing the FBG sensor and the 18650 cell was subsequently sealed with an epoxy that was cured for 24 h; all processes were performed inside the glove box whose O_2 and H_2O content was maintained less than 0.1 ppm. Cells were cycled using BCS battery cycler (Bio-Logic, France) by keeping the cells inside an oven at 55 °C, and the cycling rates were calculated on the basis of NVPF material (1C = 128 mA g^{-1}). Sensors were connected to FBGuard1550 (Safibra) or LUNA Si255 (Micron Optics) interrogator via optical fibres. The sampling period of the interrogator was set to 1 s. According

to the mentioned specifications, wavelength accurcy of the interrogators is 1pm. The FBGs were purchased from SAMYON and calibrated before use.

Calibration of FBG sensors: The temperature calibration of the FBG sensors was conducted in the temperature ovens (IPP110, Memmert) after being inserted into the 18650 cells, from 55 °C to 45 °C in 5°C increments. The thermal rate constant, k_T, was then linearly fitted according to the equation, $\Delta\lambda_B = k_T\Delta T$ with $\Delta\lambda_B$ and ΔT being the Bragg wavelength shift and the temperature change, respectively.

Calibration of optical sensing calorimetry: According to the zero-dimensional thermal model (see Figure S2a in the Supporting Information), the heat generation rate of the cell, $\dot{Q}$, can be calculated by

$$\dot{Q} = MC_P\frac{dT}{dt} + \dot{q} \tag{1}$$

where M is the mass of the cell, C_P is cell's specific heat capacity, T is the spatially average temperature of the cell, and t is the time, and $\dot{q}$ is the heat dissipation rate of the cell to the environment. T is estimated according to the geometry, the internal and the surface temperatures of the cell, see the details of the previous study[18]. The thermal model also gives

$$\dot{q} = \frac{T_{surface} - T_{ambient}}{R_{out}} \tag{2}$$

where $T_{surface}$ and $T_{ambient}$ are the temperatures at the surface of the cell and the ambient environment, respectively, and R_{out} is the equivalent thermal resistance between the cell's surface and the ambient. To calculate the $\dot{Q}$ in real time, we determined the intrinsic parameters (MC_P and R_{out}) by applying an alternative galvanostatic pulse at a frequency of 2 Hz to the cell for producing known $\dot{Q}$ (see Figure S2b in the Supporting Information), zoomed view of the pulse is presented on the right part of Figure S2b (in the Supporting Information). Namely, because the sum of the reversible entropy terms over a cycle is zero, we calculated $\dot{Q}$ by the equation, $\dot{Q} = \oint_{Cycle} IV$, where the voltage ($V$) and the current ($I$) were recorded by the potentiostat. Together with the temporal temperature data, R_{out} can be determined during the steady state (when $\frac{dT}{dt} = 0$ and thus $\dot{Q} = \dot{q}$, see Figure S2c in the Supporting Information) by

$R_{out} = \frac{T_{surface} - T_{ambient}}{\dot{q}}$ from Equation (2). In addition, MC_P was then calculated in the transient state (Figure S2c in the Supporting Information) by linearly fitting $\dot{Q} - \dot{q} = MC_P \frac{dT}{dt}$ from Equation (1), where $\dot{q}$ was computed by the determined R_{out} and Equation (2). Afterwards, we could derive $\dot{Q}$ under any electrochemical conditions according to Equations (1) and (2) by the *operando* temperature data and the pre-determined MC_P and R_{out}.

Operando pressure monitoring via optical sensors: In order to examine the *operando* pressure accumulation in different electrolyte formulae, we simultaneously inserted a FBG in a single-ring suspended microstructured optical fiber (MOF-FBG) with a high pressure sensitivity ($k_{P,MOF}$) of -2.7 pm bar^{-1} and a FBG in a single-mode fiber (SMF-FBG) with a low pressure sensitivity ($k_{P,SMF}$) of -0.3 pm bar^{-1} into the 18650, see more details in our previous work[18]. Due to the remarkable pressure sensitivity of MOF-FBG, the pressure change (ΔP) can be calculated as follows[18].

$$\Delta P = \frac{k_{T,SMF}\Delta\lambda_{B,MOF} - k_{T,MOF}\Delta\lambda_{B,SMF}}{k_{T,SMF}k_{P,MOF} - k_{T,MOF}k_{P,SMF}} \tag{3}$$

where $k_{T,SMF}$ and $k_{T,MOF}$ are the thermal rate constants of SMF-FBG and MOF-FBG, respectively, and $\Delta\lambda_{B,SMF}$ and $\Delta\lambda_{B,MOF}$ are the Bragg wavelength shifts of SMF-FBG and MOF-FBG, respectively

Electrochemical testing of NVPF and HC symmetric cell: Two NVPF-HC full cells with the same electrolyte were assembled in CR-2032 type coin cells inside an Ar-filled glovebox. Both the cells were cycled for one cycle to complete the formation of the cell. Then one of the two cells was charged to 4.3 V (constant current CC mode) and kept at 4.3 V (constant voltage CV mode) for 12 hours, another cell was kept at 2 V (CC- CV). Both the cells were removed from the cycler at the same time and then decrimped inside the glovebox. The NVPF and HC electrodes removed from cell discharged to 2 V is used as +ve NVPF (Na~$_3$V$_2$(PO$_4$)$_2$F$_3$) and -ve HC (de-sodiated HC). Similarly, NVPF and HC removed from cell charged to 4.3 V is used as -ve NVPF (Na~$_1$V$_2$(PO$_4$)$_2$F$_3$) and +ve HC (sodiated HC). The +ve NVPF/-ve NVPF and +ve HC/-ve HC symmetric cells were assembled using the aforementioned electrode with the electrolyte formulation which was used in full cells to get these electrodes. The cells were cycled at room

temperature at C/5 rate. All cells were duplicated and the results were compared only when the reproducibility was assured.

Online electrochemical mass spectrometry: Slurries comprising either 90 wt% of NVPF, 5 wt% of conductive carbon SC65, and 5 wt% of PVdF binder, or 80 wt% of HC, 10 wt% of conductive carbon SC65, and 10 wt% of PVdF binder were cast on an Al mesh and subsequently punched into electrode discs of 13 mm in diameter. In-house designed OEMS full cells were assembled in an Ar-filled glovebox with both H_2O and O_2 contents less than 0.1 ppm, using an NVPF disc as cathode, one piece of Whatman GF/D glassfibre as separator, an HC disc as anode, and 150 μL of Na-based electrolyte. The cells were cycled between 1.8 – 4.3 V inside a temperature chamber at 55 °C using a current density of 12.8 mA g^{-1}. H_2, CO_2, and C_2H_4 amounts were quantitatively measured by a quadrupole mass spectrometer (Pfeiffer, Switzerland), where the technical details can be found elsewhere[51].

Supporting Information

Supporting Information is available from the Wiley Online Library or from the author.

Conflict of interests

The authors declare no conflict of interest. The electrolyte with additives NaODFB, VC, SN and TMSPi is patented with patent application number EP21305354.9.

References

[1]   R. Schmuch, R. Wagner, G. Hörpel, T. Placke, M. Winter, *Nat. Energy* **2018**, *3*, 267.
[2]   D. Larcher, J.-M. Tarascon, *Nat. Chem.* **2015**, *7*, 19.
[3]   M. Weil, S. Ziemann, J. Peters, in *Behav. Lithium-Ion Batter. Electr. Veh. Battery Health Perform. Saf. Cost* (Eds.: G. Pistoia, B. Liaw), Springer International Publishing, Cham, **2018**, pp. 59–74.
[4]   H. Hijazi, P. Desai, S. Mariyappan, *Batter. Supercaps* **2021**, *4*, 881.
[5]   A. Bauer, J. Song, S. Vail, W. Pan, J. Barker, Y. Lu, *Adv. Energy Mater.* **2018**, *8*, 1702869.
[6]   J. Song, B. Xiao, Y. Lin, K. Xu, X. Li, *Adv. Energy Mater.* **2018**, *8*, 1703082.
[7]   K. Xu, *Chem. Rev.* **2004**, *104*, 4303.
[8]   K. Xu, *Chem. Rev.* **2014**, *114*, 11503.
[9]   X. Xia, M. N. Obrovac, J. R. Dahn, *Electrochem. Solid-State Lett.* **2011**, *14*, A130.
[10]   R. Mogensen, D. Brandell, R. Younesi, *ACS Energy Lett.* **2016**, *1*, 1173.
[11]   D. I. Iermakova, R. Dugas, M. R. Palacín, A. Ponrouch, *J. Electrochem. Soc.* **2015**, *162*, A7060.
[12]   S. S. Zhang, *J. Power Sources* **2006**, *162*, 1379.
[13]   L. Cheng, R. S. Assary, X. Qu, A. Jain, S. P. Ong, N. N. Rajput, K. Persson, L. A. Curtiss, *J. Phys. Chem. Lett.* **2015**, *6*, 283.
[14]   A. Benayad, J. E. Morales-Ugarte, C. C. Santini, R. Bouchet, *J. Phys. Chem. A* **2021**, *125*, 1069.
[15]   R. Pigliapochi, S. Benders, E. V. Silletta, S. L. Glazier, E. Lee, J. Dahn, A. Jerschow, *Batter. Supercaps* **2021**, *4*, 322.
[16]   N. M. Trease, L. Zhou, H. J. Chang, B. Y. Zhu, C. P. Grey, *Solid State Nucl. Magn. Reson.* **2012**, *42*, 62.
[17]   Y. Yuan, K. Amine, J. Lu, R. Shahbazian-Yassar, *Nat. Commun.* **2017**, *8*, 15806.
[18]   J. Huang, L. Albero Blanquer, J. Bonefacino, E. R. Logan, D. Alves Dalla Corte, C. Delacourt, B. M. Gallant, S. T. Boles, J. R. Dahn, H.-Y. Tam, J.-M. Tarascon, *Nat. Energy* **2020**, *5*, 674.
[19]   J. Chen, Z. Huang, C. Wang, S. Porter, B. Wang, W. Lie, H. K. Liu, *Chem. Commun.* **2015**, *51*, 9809.
[20]   D. Aurbach, K. Gamolsky, B. Markovsky, Y. Gofer, M. Schmidt, U. Heider, *Electrochimica Acta* **2002**, *47*, 1423.
[21]   Y.-S. Kim, T.-H. Kim, H. Lee, H.-K. Song, *Energy Environ. Sci.* **2011**, *4*, 4038.
[22]   Y.-M. Song, J.-G. Han, S. Park, K. Tae Lee, N.-S. Choi, *J. Mater. Chem. A* **2014**, *2*, 9506.
[23]   G. Yan, D. Alves-Dalla-Corte, W. Yin, N. Madern, G. Gachot, J.-M. Tarascon, *J. Electrochem. Soc.* **2018**, *165*, A1222.
[24]   C. Cometto, G. Yan, S. Mariyappan, J.-M. Tarascon, *J. Electrochem. Soc.* **2019**, *166*, A3723.
[25]   G. Yan, K. Reeves, D. Foix, Z. Li, C. Cometto, S. Mariyappan, M. Salanne, J.-M. Tarascon, *Adv. Energy Mater.* **2019**, *9*, 1901431.
[26]   R. Fong, U. von Sacken, J. R. Dahn, *J. Electrochem. Soc.* **1990**, *137*, 2009.
[27]   M. S. Ding, K. Xu, T. R. Jow, *J. Electrochem. Soc.* **2000**, *147*, 1688.
[28]   M. S. Ding, K. Xu, S. Zhang, T. R. Jow, *J. Electrochem. Soc.* **2001**, *148*, A299.
[29]   M. S. Ding, *J. Electrochem. Soc.* **2004**, *151*, A731.
[30]   F. Leng, C. M. Tan, M. Pecht, *Sci. Rep.* **2015**, *5*, 12967.
[31]   X. Zhang, R. Kostecki, T. J. Richardson, J. K. Pugh, P. N. Ross, *J. Electrochem. Soc.* **2001**, *148*, A1341.
[32]   S. Grugeon, P. Jankowski, D. Cailleu, C. Forestier, L. Sannier, M. Armand, P. Johansson, S. Laruelle, *J. Power Sources* **2019**, *427*, 77.

[33] A. L. Michan, Bharathy. S. Parimalam, M. Leskes, R. N. Kerber, T. Yoon, C. P. Grey, B. L. Lucht, *Chem. Mater.* **2016**, *28*, 8149.

[34] K. Ushirogata, K. Sodeyama, Y. Okuno, Y. Tateyama, *J. Am. Chem. Soc.* **2013**, *135*, 11967.

[35] G.-Y. Kim, J. R. Dahn, *J. Electrochem. Soc.* **2015**, *162*, A437.

[36] H. Zhi, L. Xing, X. Zheng, K. Xu, W. Li, *J. Phys. Chem. Lett.* **2017**, *8*, 6048.

[37] G.-Y. Kim, R. Petibon, J. R. Dahn, *J. Electrochem. Soc.* **2014**, *161*, A506.

[38] T. Yim, S.-G. Woo, S. H. Lim, W. Cho, J. H. Song, Y.-K. Han, Y.-J. Kim, *J. Mater. Chem. A* **2015**, *3*, 6157.

[39] Y.-K. Han, J. Yoo, T. Yim, *J. Mater. Chem. A* **2015**, *3*, 10900.

[40] I. Bloom, A. N. Jansen, D. P. Abraham, J. Knuth, S. A. Jones, V. S. Battaglia, G. L. Henriksen, *J. Power Sources* **2005**, *139*, 295.

[41] H. M. Dahn, A. J. Smith, J. C. Burns, D. A. Stevens, J. R. Dahn, *J. Electrochem. Soc.* **2012**, *159*, A1405.

[42] G. Yan, R. Dugas, J.-M. Tarascon, *J. Electrochem. Soc.* **2018**, *165*, A220.

[43] A. J. Smith, J. C. Burns, D. Xiong, J. R. Dahn, *J. Electrochem. Soc.* **2011**, *158*, A1136.

[44] E. R. Logan, H. Hebecker, X. Ma, J. Quinn, Y. HyeJeong, S. Kumakura, J. Paulsen, J. R. Dahn, *J. Electrochem. Soc.* **2020**, *167*, 060530.

[45] J. C. Burns, L. J. Krause, D.-B. Le, L. D. Jensen, A. J. Smith, D. Xiong, J. R. Dahn, *J. Electrochem. Soc.* **2011**, *158*, A1417.

[46] C. Shen, D. Xiong, L. D. Ellis, K. L. Gering, L. Huang, J. R. Dahn, *J. Electrochem. Soc.* **2017**, *164*, A3349.

[47] L. J. Krause, L. D. Jensen, J. R. Dahn, *J. Electrochem. Soc.* **2012**, *159*, A937.

[48] J.-Y. Eom, I.-H. Jung, J.-H. Lee, *J. Power Sources* **2011**, *196*, 9810.

[49] X. Qi, L. Tao, H. Hahn, C. Schultz, D. R. Gallus, X. Cao, S. Nowak, S. Röser, J. Li, I. Cekic-Laskovic, B. R. Rad, M. Winter, *RSC Adv.* **2016**, *6*, 38342.

[50] M. Metzger, B. Strehle, S. Solchenbach, H. A. Gasteiger, *J. Electrochem. Soc.* **2016**, *163*, A798.

[51] M. He, Elucidating Interface Reactions in Li-Ion Batteries and Supercapacitors by in Situ Gas Analysis, Doctoral Thesis, ETH Zurich, **2016**.

Table of content entry:

In-depth understanding of interfacial reactions between electrode and electrolyte can be achieved using *operando* monitoring of thermal events during interphase formation using optical sensors. The present study set an example for such analyses that together with complementary electrochemical analyses lead to identification of optimized electrolyte formulation for Na-ion batteries.

Parth Desai, Jiaqiang Huang, Hussein Hijazi, Leiting Zhang, Sathiya Mariyappan,[*] and Jean-Marie Tarascon[*]

Deciphering interfacial reactions via optical sensing to tune the interphase chemistry for optimized Na-ion electrolyte formulation

ToC figure:
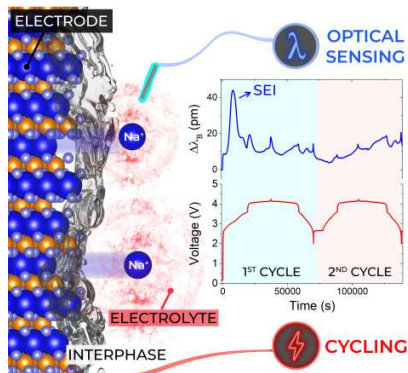
Supporting Information

Deciphering interfacial reactions via optical sensing to tune the interphase chemistry for optimized Na-ion electrolyte formulation

*Parth Desai, Jiaqiang Huang, Hussein Hijazi, Leiting Zhang, Sathiya Mariyappan,[*] and Jean-Marie Tarascon[*]*

Supporting Figures.
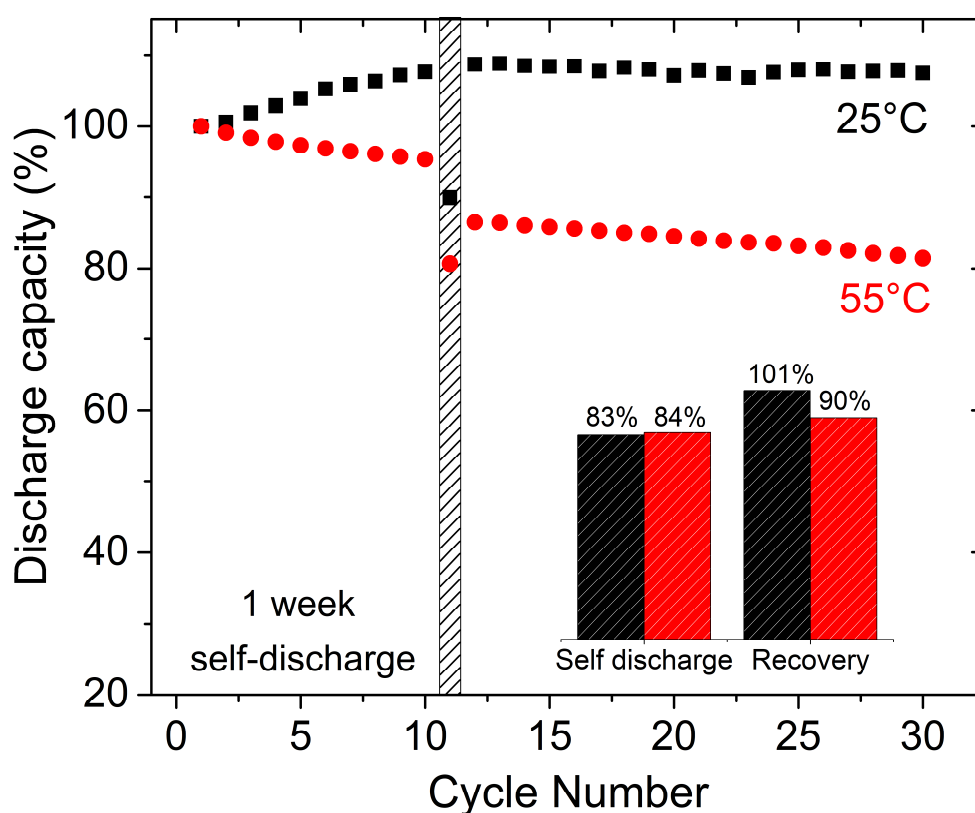
Figure S1. The percentage capacity retention *vs.* cycle number for $Na_3V_2(PO_4)_2F_3$ (NVPF) / hard carbon (HC) full cells using 1M $NaPF_6$ in EC: PC: DMC (1:1:1 by volume) as electrolyte. The cells were cycled at C/5 in a fixed temperature of 25°C and 55°C by keeping them in an oven maintained at the required temperature. The cells were cycled for 10 cycles after which allowed to rest (self-discharge test) at 100% SOC (4.3V) for 1 week. Discharge capacity of 10th, 11th and 12th cycle is Q_{10}, Q_{11} and Q_{12} respectively. The percentage capacity observed just after self-discharge (Q_{11}/Q_{10}) and in recovery cycle (Q_{12}/Q_{10}) is presented in the histogram as inset in the Figure S1. Stable capacity retention with 100 % recovery was observed at 25 °C, while pronounced capacity decay with solely 90 % recovery after self-discharge test was obtained at 55 °C indicating the comparatively poor performance of the electrolyte at high temperature cycling.
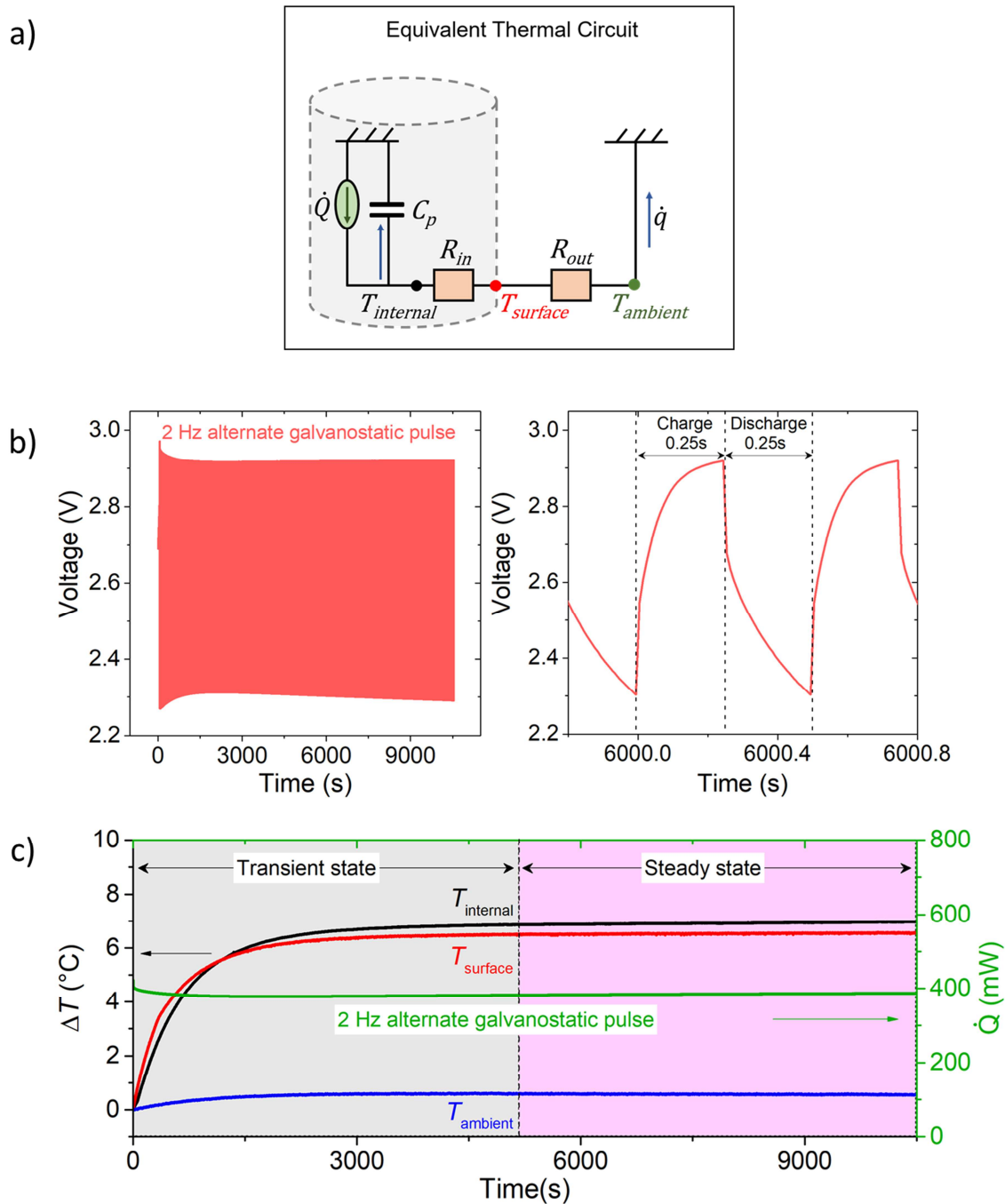
Figure S2. (a) Thermal equivalent circuit for zero dimensional thermal model used for sensing calorimetry. (b) The voltage *vs.* time behavior of NVPF/HC cylindrical 18650 cell during the alternative galvanostatic pulse at a frequency of 2 Hz is shown for the complete data (b, left) and for one full cycle (b, right). Applied current gives the rate of heat generation ($\dot{Q}$) and is calculated as $\dot{Q} = \oint_{Cycle} IV$. (c) Thermal response corresponding to the applied galvanostatic pulse for ambient, surface and internal sensors. Temperature response is divided into transient state and steady state. R_{out} is determined from steady state and then MC_P (~38 J K^{-1}) is calculated from the transient state (See *Calibration of optical sensing calorimetry* in Experimental Procedure for details).
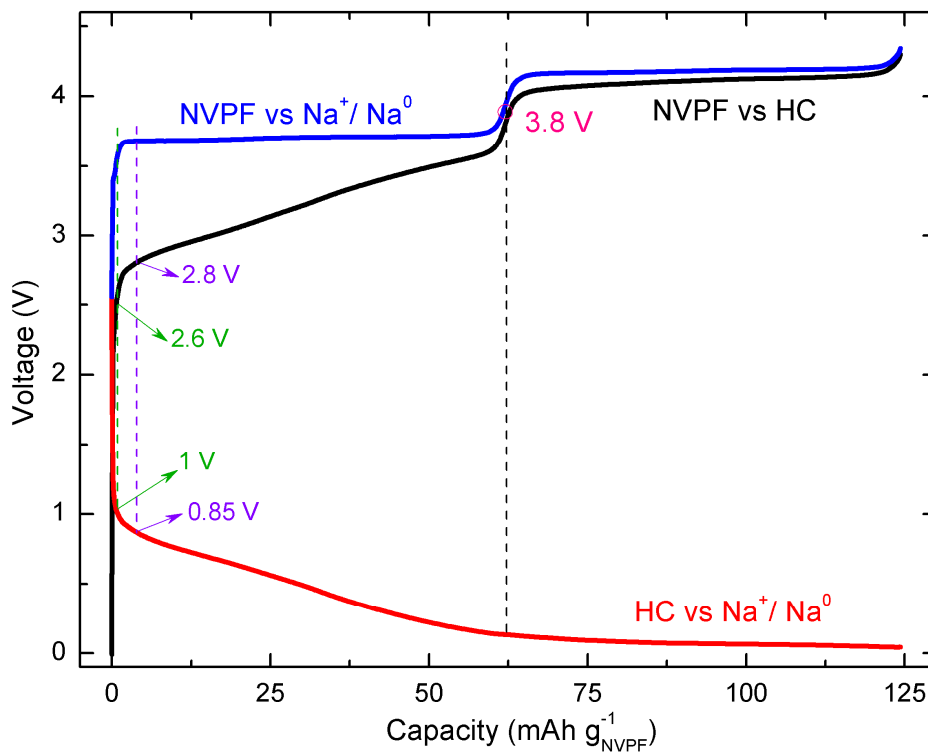
Figure S3. The three electrode cycling data of NVPF/HC cell where the cell was cycled using NVPF and HC as positive and negative electrodes respectively while a piece of sodium metal is used as the reference electrode. The black curve shows the potential evolution of the NVPF/HC cell as a function of capacity whereas blue and red curves represent the corresponding potential of individual electrodes (NVPF and HC) measured against sodium metal. For example, 2.6 V and 2.8 V in the NVPF/HC full cell nearly corresponds to 1 V and 0.85 V of HC versus Na. Similarly, the 3.8 V in NVPF/HC cell corresponds to 1 sodium removal from NVPF. The capacity is measured with respect to the active material weight of NVPF. (Related to Figure 2)
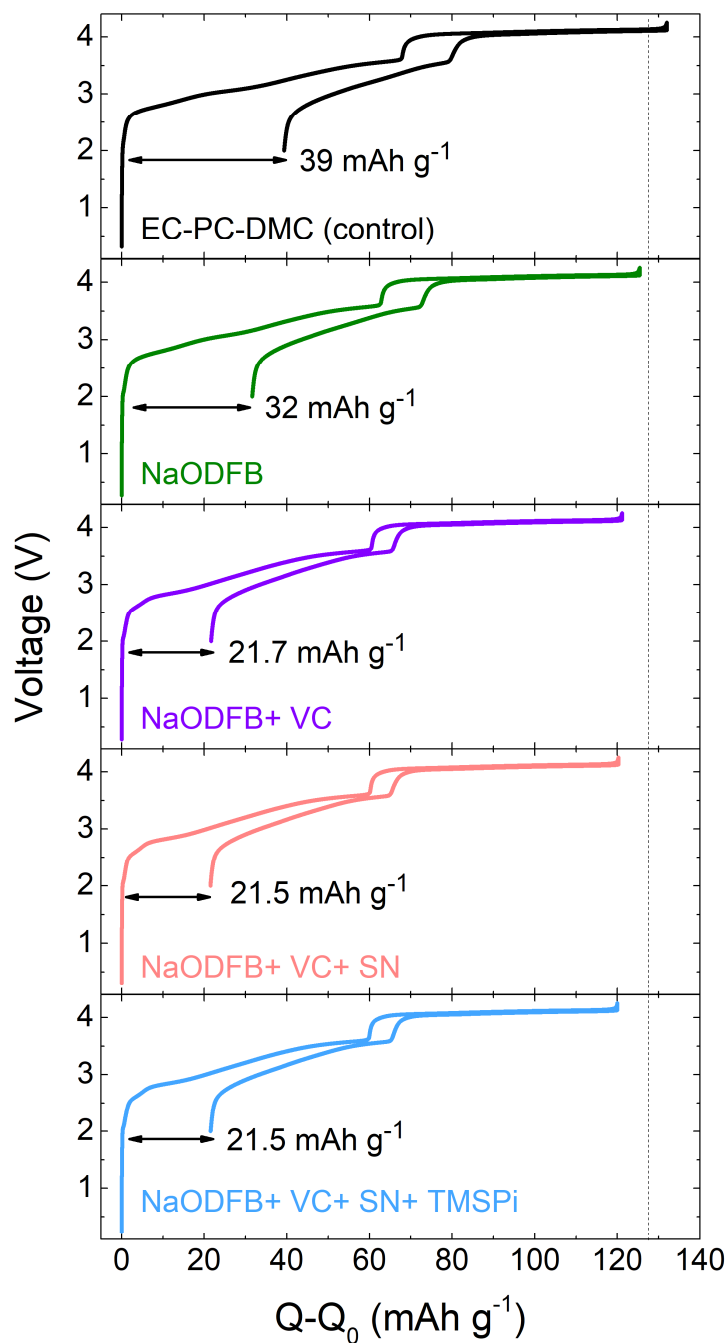
Figure S4. The 1st cycle data of NVPF/HC cylindrical 18650 cells used for the sensing studies. Minimum 2 cells were assembled for each electrolyte formulation and the cells are kept in 55 °C oven and cycled at C/10 rate. The electrolyte studied are the control electrolyte (1 M $NaPF_6$ in EC- PC- DMC 1: 1: 1 by volume) with no additive or having additives namely 0.5 wt% NaODFB, 0.5 wt% NaODFB+ 3 wt% VC, 0.5 wt% NaODFB+ 3 wt% VC+ 3 wt% SN and 0.5 wt% NaODFB+ 3 wt% VC+ 3 wt% SN+ 0.2 wt% TMSPi respectively. The mentioned additive combinations are blended in control electrolyte and named using the additives present in that specific electrolyte formulation. The first cycle irreversible capacities are mentioned in the figures. The dotted line in the figure indicates the theoretical capacity limit of the cell. (Related to Figure 2).
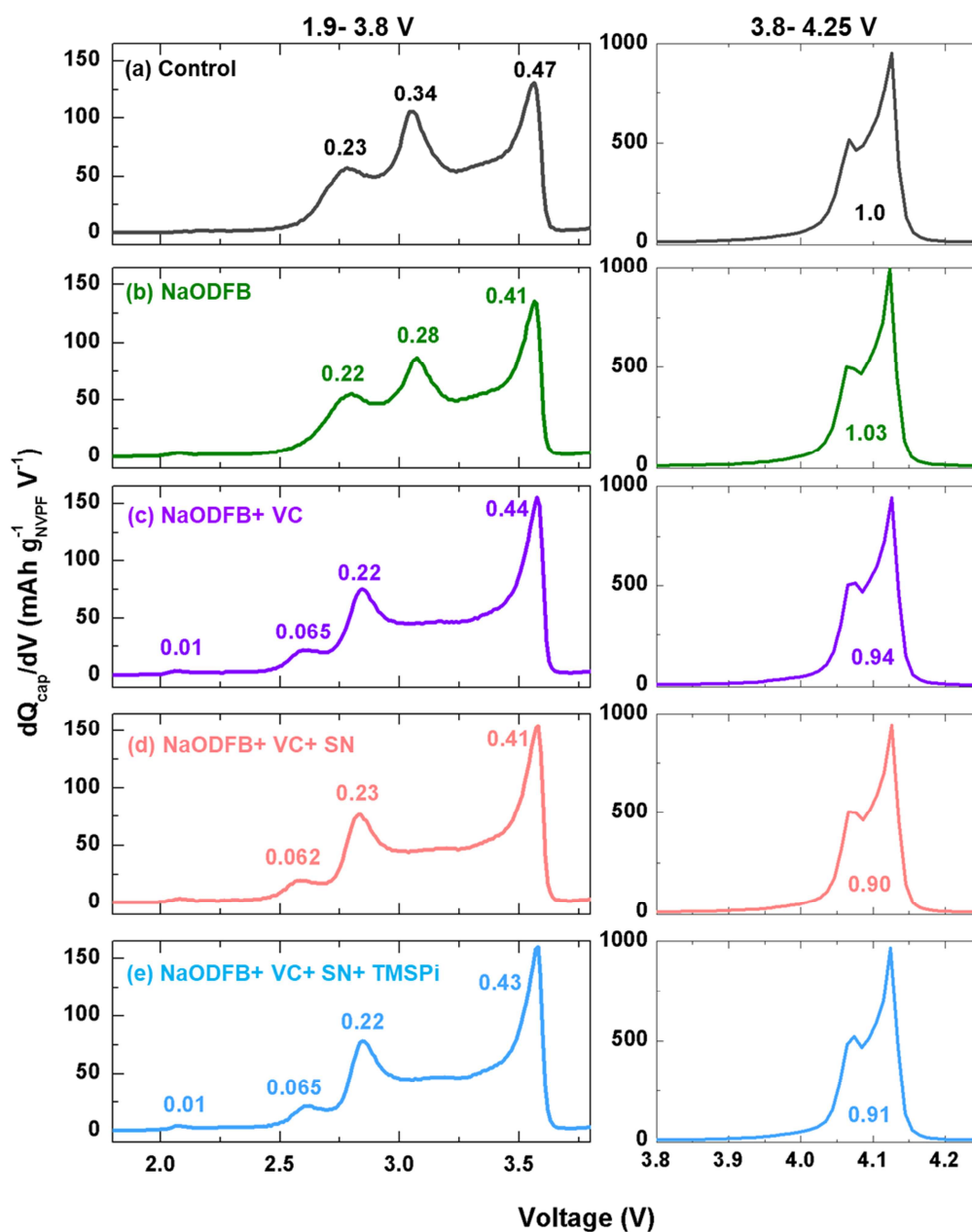
Figure S5. Capacity derivative dQ_{cap}/dV *vs.* voltage (V) plots for the 1st charge of the NVPF/HC cylindrical 18650 cells. The voltage region from OCV- 3.8 V are shown in left and 3.8- 4.25 V in right. The electrolyte studied are the control electrolyte (1 M NaPF$_6$ in EC- PC- DMC 1: 1: 1 by volume) with no additive or having additives namely 0.5 wt% NaODFB, 0.5 wt% NaODFB+ 3 wt% VC, 0.5 wt% NaODFB+ 3 wt% VC+ 3 wt% SN and 0.5 wt% NaODFB+ 3 wt% VC+ 3 wt% SN+ 0.2 wt% TMSPi respectively. Amount of e[-] involved in the reaction corresponding to a particular peak is presented in the figure and is calculated with respect to NVPF. (Related to Figure 2)
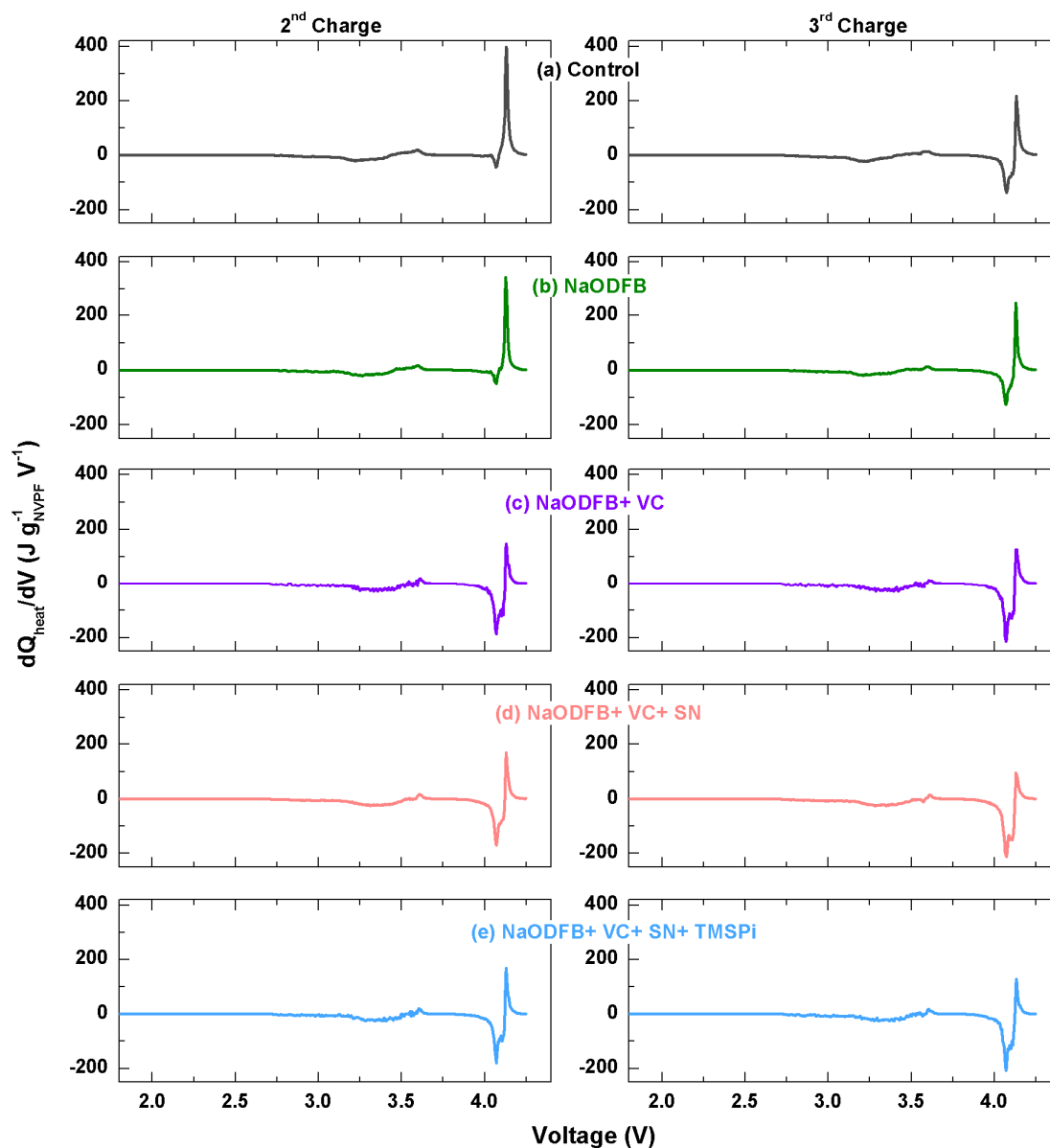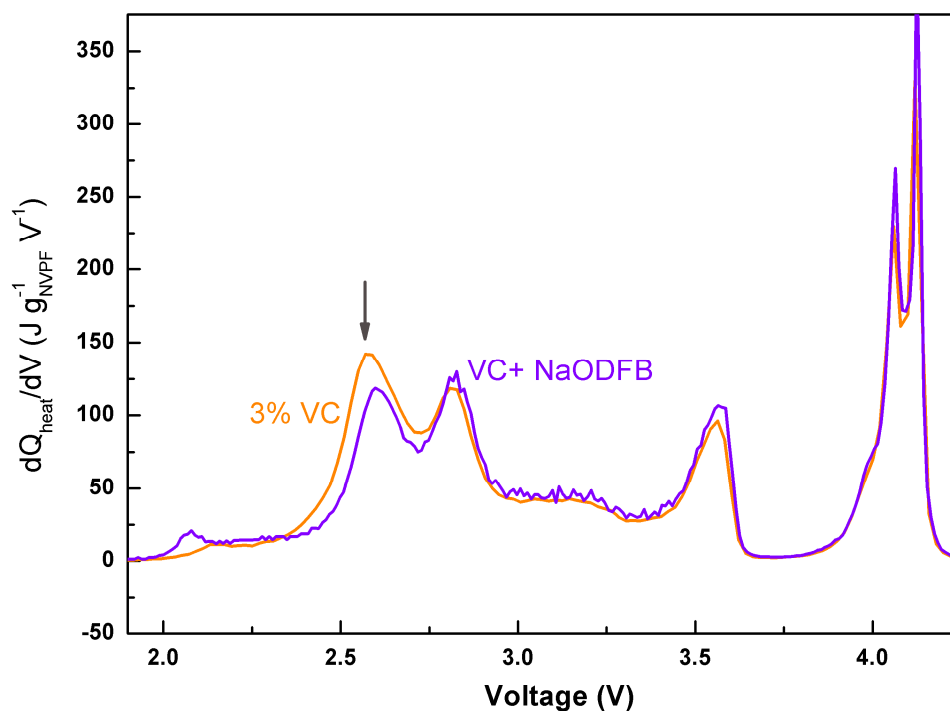
Figure S6. Derivative heat dQ_{heat}/dV *vs.* voltage (V) plots for the 2nd and 3rd charge of the NVPF/HC cylindrical 18650 cells cycled at C/10 in 55°C oven. The electrolyte studied are the control electrolyte (1 M $NaPF_6$ in EC- PC- DMC 1: 1: 1 by volume) with no additive or having additives namely 0.5 wt% NaODFB, 0.5 wt% NaODFB+ 3 wt% VC, 0.5 wt% NaODFB+ 3 wt% VC+ 3 wt% SN and 0.5 wt% NaODFB+ 3 wt% VC+ 3 wt% SN+ 0.2 wt% TMSPi respectively. A clear evolution in exothermic heat was observed in moving from 2nd charge to 3rd charge, especially above 3.8 V; however the evolutions are minimum in (c), (d) and (e) indicating faster stabilisation of positive electrode in these electrolytes. (The data were derived from same cells whose first charges were shown in supporting Figure S4, S5 and Figure 2.)
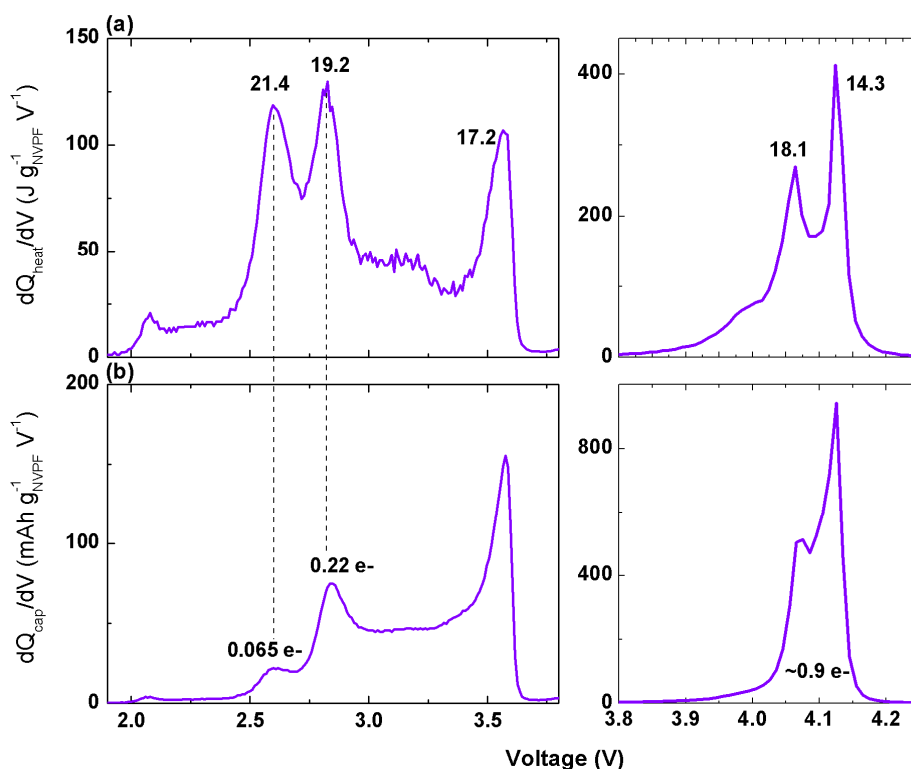
Figure S7. Comparison of derivative heat (dQ_heat/dV) with derivative capacity (dQ_cap/dV) as a function of potential (V) for the NVPF/HC cylindrical 18650 cells using 1M NaPF_6 in EC- PC- DMC (1: 1: 1 by volume) with additives NaODFB+ VC. The cells were cycled at 55°C using C/10 rate. The total heats (in joules per gram of NVPF) for each exothermic peak were measured by integrating the total area under the peak and are mentioned in (a). Similarly, the corresponding electrons involved were measured from the capacity obtained in that voltage region and converting them to ΔNa, hence electrons (e⁻). The heat evolution peaks at 2.6 V and 2.8 V have almost similar area but the corresponding e⁻ involved at 2.6 V are less than that at 2.8 V, indicating the process at 2.6 V is highly exothermic chemical/ electrochemical reaction. (Related to Figure S2c)

Figure S8. The heat derivatives dQ$_{heat}$/dV *vs.* V of NVPF/ HC cylindrical 18650 cells cycled at 55 °C. The data from two different electrolyte formulations were compared in which one electrolyte was 1 M NaPF$_6$ in EC-PC-DMC (1 :1: 1 by volume) with solely 3 wt% VC as additive and the other one had 0.5 wt% NaODFB+ 3%VC. In short, both electrolytes differ only by presence or absence of NaODFB additive. Relatively lesser heat was observed at 2.6 V process when VC is used together with NaODFB indicating the possible suppression of VC reduction by the addition of NaODFB. (Related to Figure S2c)
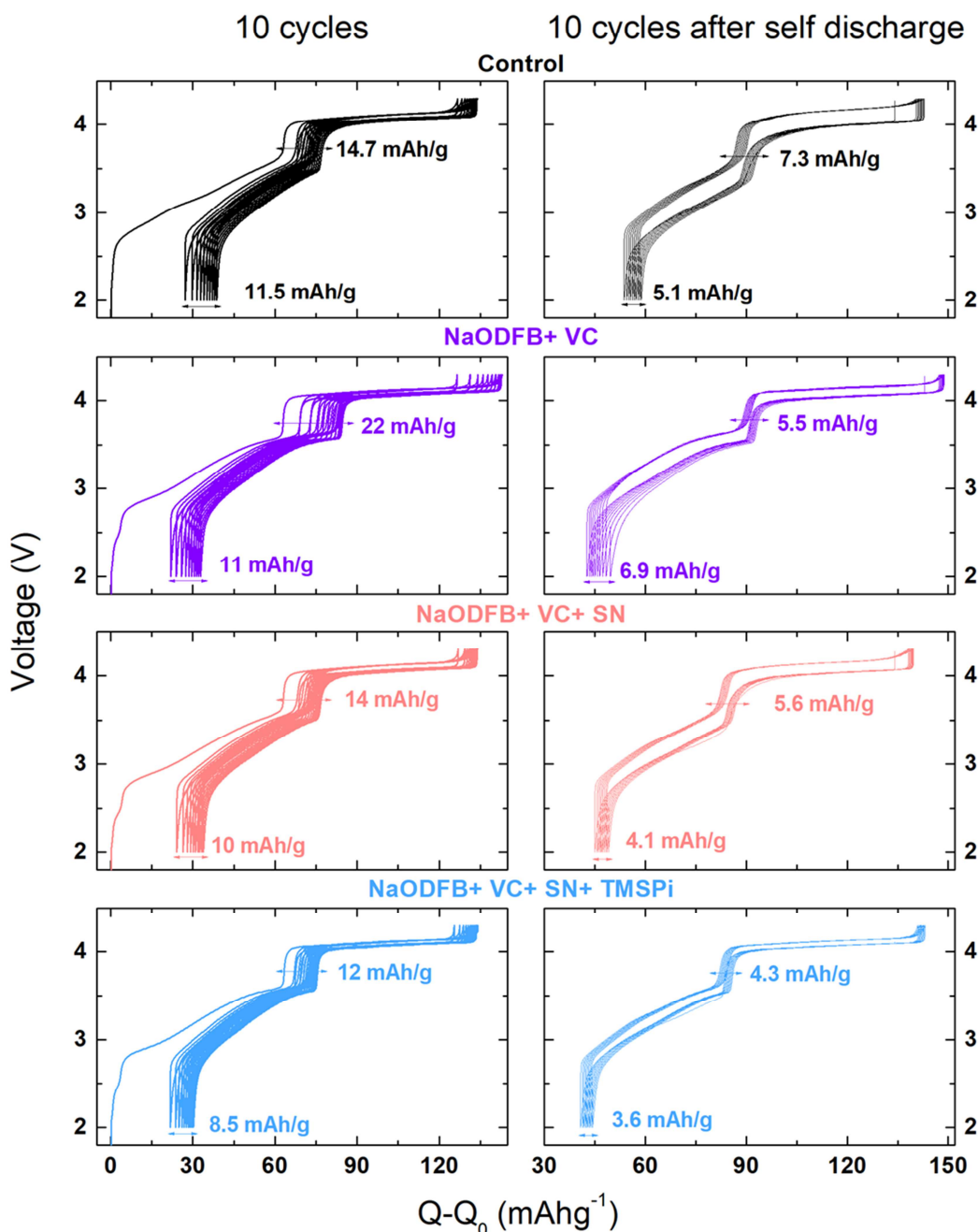
Figure S9. Voltage *vs.* capacity (Q-Q$_0$) of NVPF/HC coin cells cycled with different electrolyte formulations at 55 °C. The cells were cycled for 10 cycles at C/5 rate and allowed to rest during the 11th charge at 4.3 V (100 % SOC) for 1 week. The cycling curves for the initial 10 cycles and the next 10 cycles after self-discharge tests were cumulated in left and right. The consolidated parameters such as capacity loss and change in polarisation during self-discharge, capacity retention are reported in Figure 3. Capacity losses happening at end of discharge and at around 50% SOC are marked in the Figure. Feature at 50 % SOC is the signature of NVPF and changes in that feature is directly correlated to the slippage of NVPF. The least capacity loss was observed with electrolyte containing 4 additives NaODFB+ VC+ SN+ TMSPi.
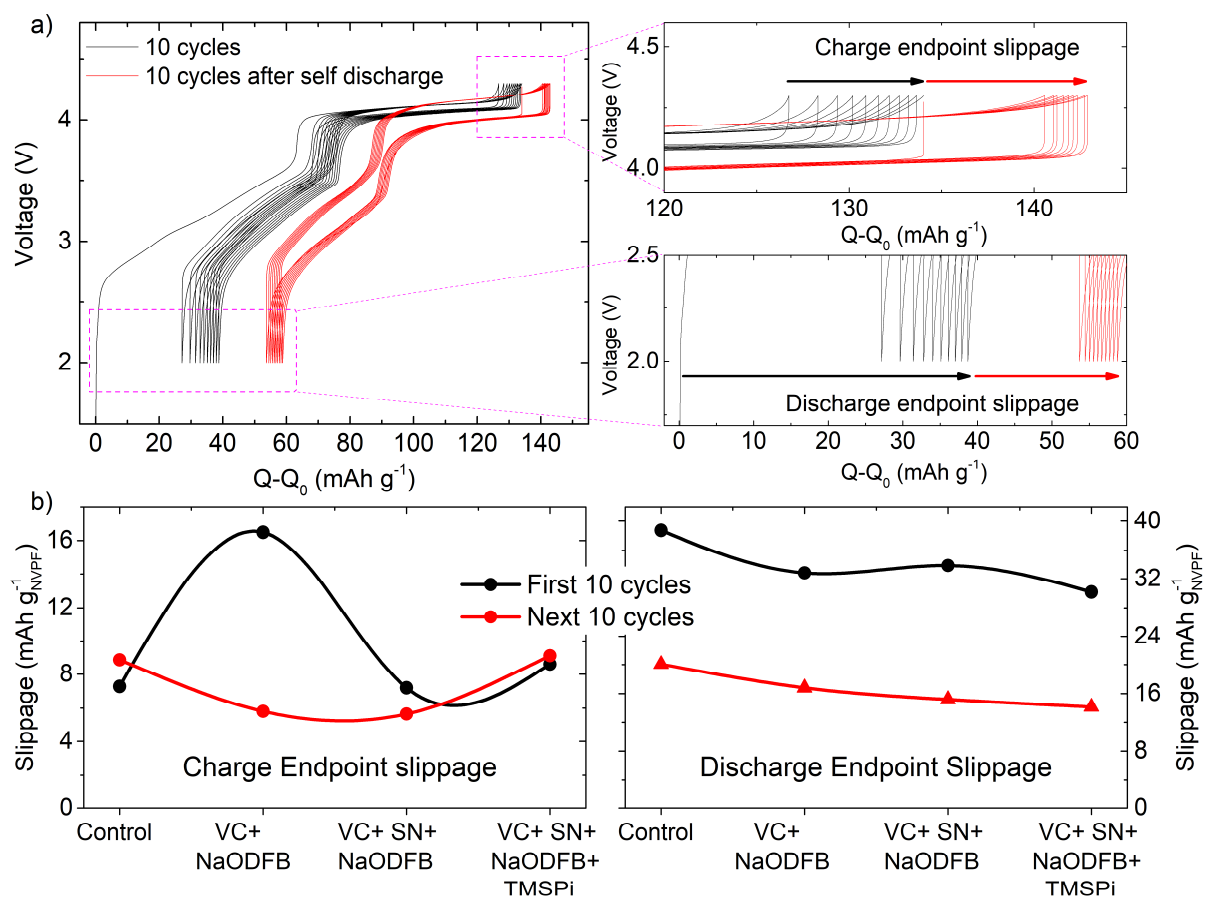
Figure S10. The end point slippage capacity in charge and discharge are measured as shown in Figure S10(a). The values for 10 cycles were calculated together to minimize the experimental error. The values thus calculated before and after self-discharge for various cells using different electrolyte formulations were consolidated in Figure S10(b). Highest end point slippage in charge is observed with electrolyte containing NaODFB+ VC specifying its poor oxidative stability. Such end point slippage is reduced with the addition of SN and TMSPi. Still, a small increase in both charge and discharge end point slippage capacity is observed with NaODFB+ VC+ SN+ TMSPi than that of the electrolyte without TMSPi (NaODFB+ VC+ SN). It could be related to the oxidation of TMSPi or its reduction product in the positive electrode.
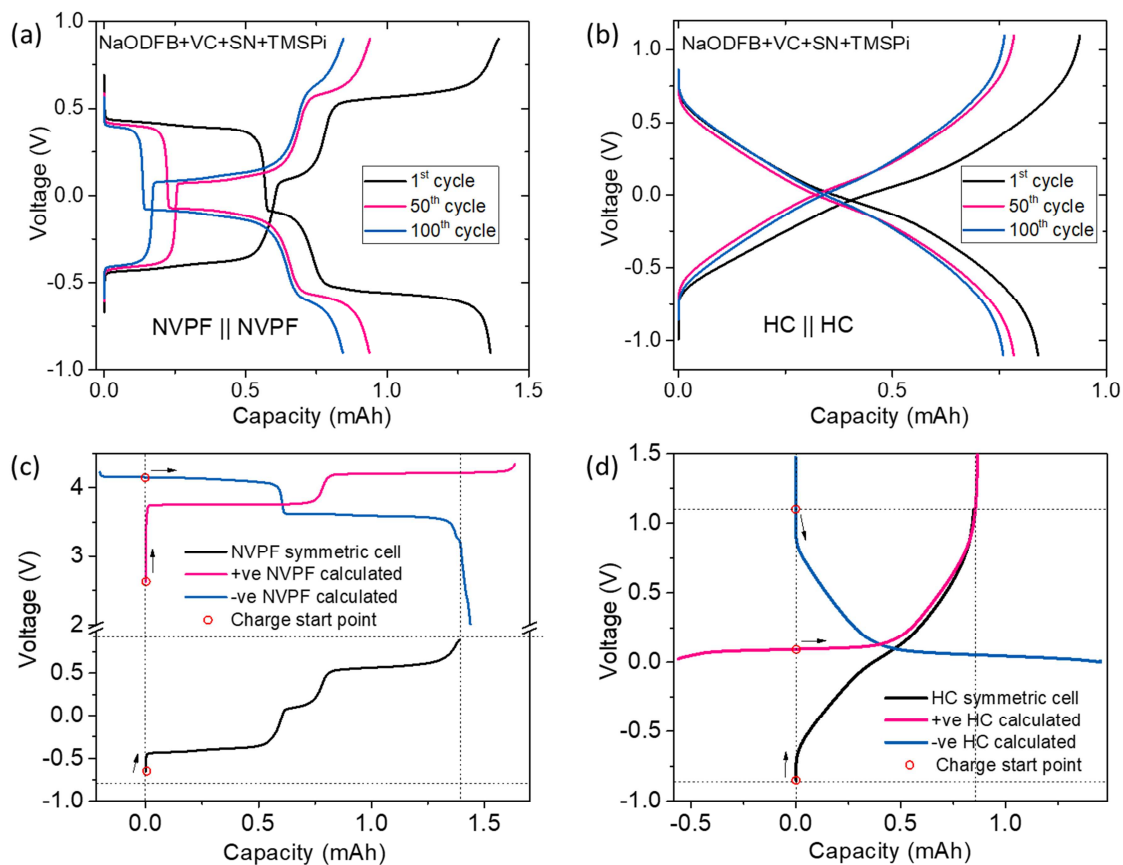
Figure S11. Galvanostatic curves for 1st, 50th and 100th cycle of (a) NVPF and (b) HC symmetric cells with NaODFB+ VC+ SN+ TMSPi electrolyte and cycled at C/5 rate at room temperature. The observed three plateau profile, in contrast to two plateau profile for NVPF material is unanticipated. But, the dV/dQ fitting performed using the software[1] developed by Dahn et al., helped us to identify the individual electrode curves. The 1st cycle charging curve is fitted using dV/dQ software and is presented for (c) NVPF and (d) HC. In the fitted curves the red circles shows the starting point of the charge for symmetric cell and individual electrodes. With the knowledge of the V(Q) profile of +ve and -ve NVPF it is much easier to visualize the shape of the symmetric cell curve since $V(Q)_{NVPF\ symmetric\ cell} = V(Q)_{+ve\ NVPF} - V(Q)_{-ve\ NVPF}$. The same goes for HC symmetric cells i.e. $V(Q)_{HC\ symmetric\ cell} = V(Q)_{+ve\ HC} - V(Q)_{-ve\ HC}$. These deconvoluted V vs Q curves for different cycles can provide the potential information about the reactions happening at the electrodes. (Related to Figure 5)
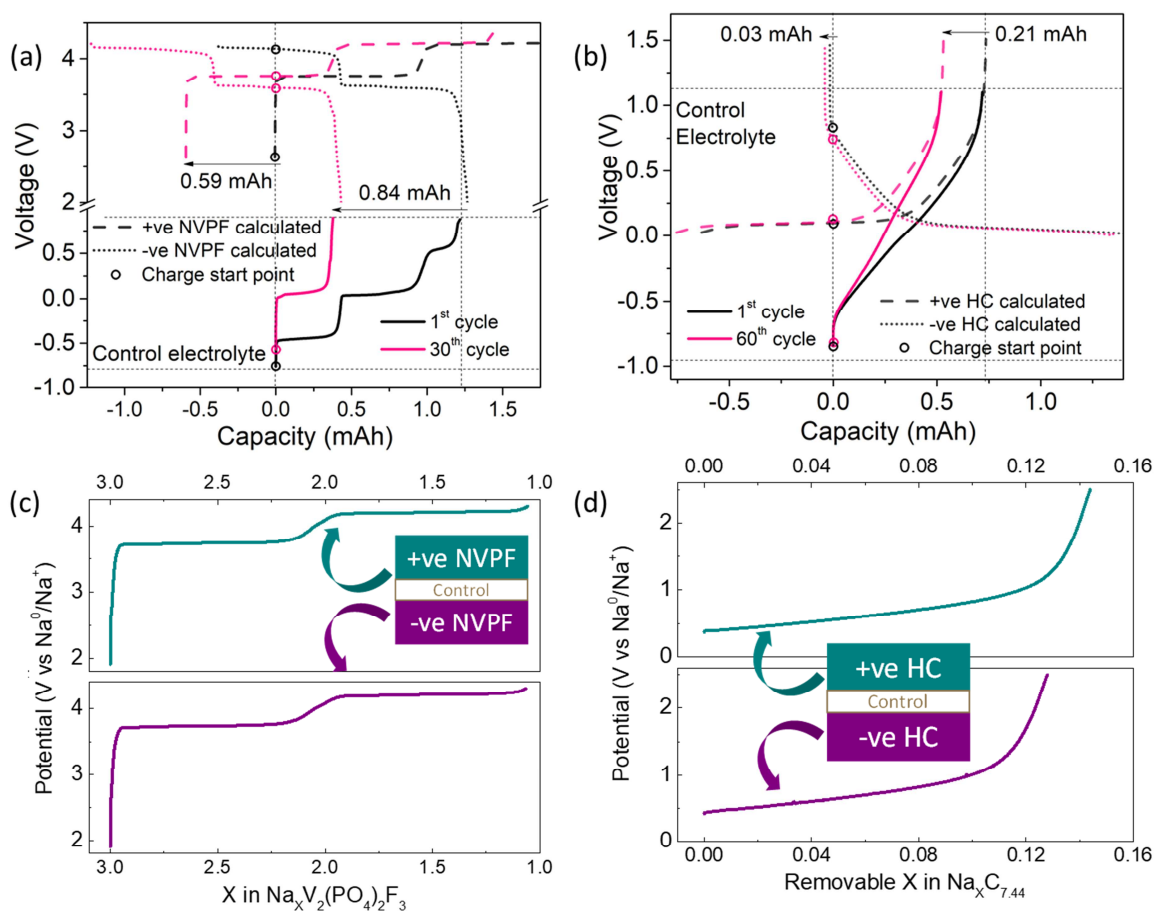
Figure S12. (a) The 1st and 30th cycle of NVPF symmetric cells with control electrolyte and the fitted +ve NVPF (dahshed) and –ve NVPF (dotted) curves. Electrode slippage at –ve NVPF(0.84 mAh) and +ve NVPF(0.59 mAh) is indicated. After 100 cycles, NVPF symmetric cell was decrimped and +ve NVPF/Na and –ve NVPF/Na half cells were prepared and sodium was extrated from NVPF, (c) shows the half cell curves. To our surprise both the NVPF had almost 3 sodium.(b) The 1st and 30th cycle of HC symmetric cells with control electrolyte and the fitted +ve HC (dashed) and –ve HC (dotted) curves. In this case slippage of +ve HC (0.21 mAh) is significantly higher than the -ve HC (0.03 mAh). After 100 cycles, HC symmetric cell was decrimped and +ve HC/Na and –ve HC/Na half cells were prepared and sodium was extrated from HC, (d) shows the half cell curves. Total Na$^+$ in the HC electrodes is 0.27 (where x=1 corrosponds to 300mAh/g of capacity for Na$_X$C$_{7.44}$).

Supporting Notes.

Note S1. To make symmetric cells, both the NVPF and HC electrodes are sodiated or desodiated as per the requirement (explained in Experimental Procedure), in NVPF/ HC full cells using the electrolyte formulation under study. The cells are decrimped and the electrodes recovered and used without washing the formed SEI/CEI. The desodiated NVPF (-ve NVPF) in Figure S11c doesn't start with composition $Na_1V_2(PO_4)_2F_3$, but with slightly more sodium. Similarly, Sodiated HC starts with the less sodium than it was sodiated (Figure S12d). After many experimental trials, it was observed that it was impossible to completely avoid this behaviour. The possible reason of this behaviour could be the process of decrimping the cell and assembling it again with fresh electrolyte. Since sodiated HC and desodiated NVPF materials are highly reactive they will try to lose and gain sodium, respectively.

Note S2. In Figure S12a the slippage at –ve electrode is 0.84 mAh which is more than the slippage at +ve electrode, 0.59mAh. Refereing to the starting point of fitted curves, –ve NVPF and +ve NVPF slippage is attributed to the gain and loss of Na^+ respectively, considering there is no mass loss. The same behaviour of –ve NMC slippage more than +ve NMC slippage can be observed in NMC symmetric cells[2]. This indicates that there is increase in the total sodium content in the electrode.To confirm this, after 100 cycles, NVPF symmetric cell was decrimped and +ve NVPF/Na and –ve NVPF/Na half cells were prepared and sodium was extrated from NVPF(shown in Figure S12c), to our surprise both the NVPF had almost 3 sodium. This indicates gain of sodium from electrolyte, which happens with simultaneous oxidation of electrolyte. Since both NVPF electrodes are at high voltage, the possibility of electrolyte reduction is negligible, hence the only dominant mechanism of degradation is electrolyte oxidation. This eliminates the cross talk caused by the reaction of reduced and oxidized species on cathode and anode electrode respectively. From the slippage of the individual electrode curves, it is established that the additive which decreases the extent of electrolyte oxidation decreases the slippage in the electrode and hence stabilizes symmetric cell capacity. (related to Figure S12a, S12c and Figure 5)

Note S3. In Figure 12b) the slippage of +ve HC (0.21 mAh) is significantly higher than the -ve HC (0.03 mAh). Refering to the starting point of fitted curves, it is evident that slippage at +ve HC and –ve HC stems from Na^+ loss and Na^+ gain respectively,considering there is no mass loss. To confirm this, after 100 cycles, HC symmetric cell was decrimped and +ve HC/Na and –ve HC/Na half cells were prepared and sodium was extrated from HC (shown in Figure S12d). Total extracted Na^+ in the HC electrodes is 0.27 (where x=1 corrosponds to 300mAh/g of capacity for $Na_XC_{7.44}$). Initial Na^+ amount after sodiation of HC for symmetric cells was 0.63(calculated from the capacity obtained in the first cycle of symmetric cell). This indicates loss of sodium to electrolyte with simultaneous electrolyte reduction and SEI growth. Since both HC electrodes are at low voltage, so the possibility of electrolyte oxidation is negligible. (related to Figure S12b, S12d and Figure 5)

References.

1. Dahn HM, Smith AJ, Burns JC, Stevens DA, Dahn JR. User-Friendly Differential Voltage Analysis Freeware for the Analysis of Degradation Mechanisms in Li-Ion Batteries. J Electrochem Soc. 2012 Aug 14;159(9):A1405.

2. Shen C, Xiong D, Ellis LD, Gering KL, Huang L, Dahn JR. Using the Charge-Discharge Cycling of Positive Electrode Symmetric Cells to Find Electrolyte/Electrode Combinations with Minimum Reactivity. J Electrochem Soc. 2017 Nov 2;164(13):A3349.